FULL PAPER

New absolute paleomagnetic intensity data from Cenozoic basalts of Northeast China and exploring rock-magnetic parameters for efficient sample preselection on the Tsunakawa–Shaw paleointensity method

Hyeon-Seon Ahn[1*] , Youn Soo Lee[2] and Yuhji Yamamoto[3]

Abstract

Despite being essential in determining absolute paleomagnetic field intensity (API) with high fidelity over Earth science research topics, API determination still suffers little quantitative success. This is due to common nonideal magnetic behaviors in experiments using natural rocks caused by physiochemical changes in the magnetic minerals contained. Although linking rock-magnetic parameters to API results may be fundamental, negligible effort has been made using the Tsunakawa–Shaw (TS) API method despite its potentially high experimental success rate in overcoming nonideal magnetic effects. Here, we explore the relationships between rock-magnetic parameters retrieved using relatively rapid and widely pre-conducted measurements and TS API results from late Cenozoic basaltic rocks. We selected rock-magnetic parameters quantified from strong-field high-temperature thermomagnetic curves, magnetic hysteresis loops, and back-field isothermal remanent magnetization demagnetizations. We provide new data pairs of rock-magnetic parameters and TS API results for 41 basaltic rock samples from 8 sites (cooling units) in Northeast China. Then, by compiling them with published data of similar quality, we compiled 133 pairs of rock-magnetic and TS API data at the sample level (38 sites). Using this data compilation, the following topics of interest were identified: Magnetic coercivity (B_c) and remanence coercivity (B_{cr}) among the hysteresis parameters, and the thermomagnetic parameter $ITC_{|m|}$ (an index of thermal change quantifying an average of the differences in saturation magnetization at a full temperature range of during a single heating–cooling run) allow meaningful and efficient discrimination between data subsets divided by "success" or "failure" in the API results. We propose sample preselection criteria for the TS experiment: a minimal set of $B_c \geq 13$ mT (or $B_{cr} \geq 26$ mT) and $ITC_{|m|} \leq 0.15$. Moreover, extended consideration based on the preselection criteria may allow the screening of potentially biased specimen/sample-level API estimates in the site-averaged determination of such a site with a large within-site API dispersion.

Keywords Paleomagnetism, Paleointensity, Tsunakawa–Shaw method, Rock-magnetic parameters, Magnetic hysteresis, Thermomagnetic analysis, Cenozoic basalts, Northeast China, Baengnyeong Island, Ethiopian Afar

*Correspondence:
Hyeon-Seon Ahn
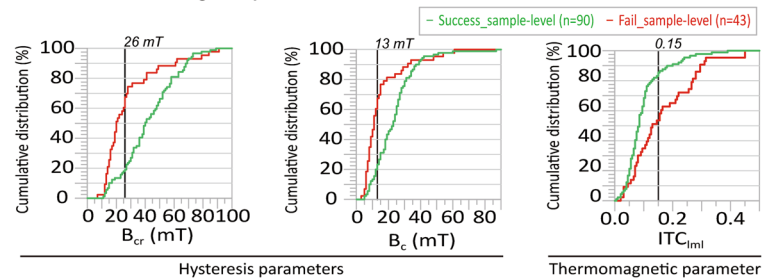mitsuki_ahs@hotmail.com; hs.ahn.86@kigam.re.kr
Full list of author information is available at the end of the article

Ahn *et al. Earth, Planets and Space* (2024) 76:9
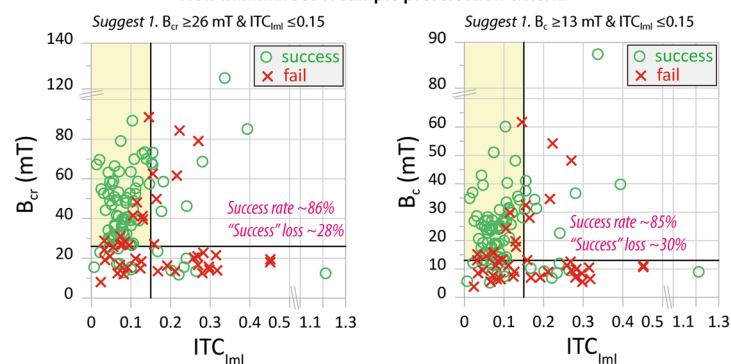
Page 2 of 29

Graphical Abstract

< Distributions in "ease-of-use" rock-magnetic parameters between the "success" and "failure" Tsunakawa-Shaw API data sets >

Introduction

The intensity of the ancient Earth's magnetic field (commonly called "paleointensity") is a crucial factor for understanding the geodynamo evolution (particularly during the early Earth's history) (Tarduno et al. 2015; Zhang et al. 2022), deep interior evolution (Bono et al. 2019; Zhou et al. 2022), and its links with surface climate, environment, and possibly other integral parts of the Earth's system (Courtillot et al. 2007; Knudsen and Riisager 2009; Lee and Kodama 2009; Kitaba et al. 2012, 2017; Suter et al. 2014; Cooper et al. 2021). The absolute estimate of paleointensity (i.e., absolute paleointensity, API) can be used in the numerical dating of volcanic activities, archeological artefacts, and remains (Pérez-Rodríguez et al. 2019; Nitta et al. 2020; Genevey et al. 2021). API can be obtained from the natural remanent magnetization (NRM) retained by the acquisition mechanism of thermoremanent magnetization (TRM) (Nagata 1953; Nagata et al. 1963) in materials such as burnt archeological artefacts, volcanic rocks, and other igneous rocks. The Thellier method, made in blocking temperature space, was proposed by Thellier and Thellier (1959) for determining APIs. Subsequently, several modifications of the method (hereafter referred to as Thellier-type methods) have been suggested and applied (Coe 1967;

Coe et al. 1978; Prévot et al. 1985; Aitken et al. 1988; Riisager and Riisager 2001; Yu et al. 2004; Wang and Kent 2013). Thellier-type methods are widely applied. However, owing to the frequent failures in API determination considering the high fidelity of the Thellier-type methods, various alternative methods have been developed and improved, for example, the Tsunakawa–Shaw (Yamamoto et al. 2003), Microwave (Hill and Shaw 2000), Triaxe (Le Goff and Gallet 2004), and Multi-specimen (Dekkers and Böhnel 2006) methods. Such API determination remains complicated because it is a time-consuming experimental procedure, exhibits complicated (nonideal) behaviors in the resultant data, and is highly dependent on the materials used (their magnetic properties that govern TRM acquisition), leading to failure in high-fidelity determination. Moreover, an array of determination criteria using multiple statistics (see Paterson et al. 2014 for the types and definitions) has been applied and has become increasingly stringent in the analysis of individual API results to avoid erroneous API data and identify more reliable API data (Kissel and Laj 2004; Leonhardt et al. 2004; Paterson et al. 2014; Cromwell et al. 2015; Tauxe et al. 2016; Sánchez-Moreno et al. 2020).

Efforts have been made to evaluate the relationships between the API results and fundamental rock-magnetic

Ahn *et al. Earth, Planets and Space* (2024) 76:9

Page 3 of 29

properties that were mainly retrieved from separate pre-conducted measurements for the efficient preselection of samples for high-fidelity API determination (Calvo et al. 2002; Carvallo et al. 2006; Wang and Kent 2013; Di Chiara et al. 2017; Paterson et al. 2017; Jeong et al. 2021; Pérez-Rodríguez et al. 2022; Fukuma 2023). These pre-conducted measurements, hysteresis measurements of saturation (M_s) and remanent (M_{rs}) magnetizations, and coercivity (B_c), combined with back-field demagnetization of saturation remanence measurement (allowing determination of remanence coercivity B_{cr}) (Calvo et al. 2002; Carvallo et al. 2006; Wang and Kent 2013; Chiara et al. 2017; Paterson et al. 2017; Jeong et al. 2021; Fukuma 2023), thermal change in magnetic susceptibility (k) or hysteresis data from before to after heating (Haag et al. 1995; Tanaka and Kono 2002; Smirnov and Tarduno 2003; Mochizuki et al. 2004; Wang and Kent 2013; Kim et al. 2018; Jeong et al. 2021), and thermomagnetic analysis that monitors thermal variation in k or induced saturation magnetization (M_s) (Haag et al. 1995; Tanaka et al. 2007; Pérez-Rodríguez et al. 2022) are the most extensively used and investigated because of the measurement speed and minimal specimen amounts needed. A comparison of the ratio combinations retrieved from the hysteresis data, that is, M_{rs}/M_s (squareness) and B_{cr}/B_c (Day et al. 1977), is known to be sensitive to the magnetic domain state, although it is influenced by other factors such as magnetic interactions, mineralogy, and thermal fluctuations (Paterson et al. 2017; Roberts et al. 2018a). Paterson et al. (2017) suggested a measure of relative bulk domain stability (BDS), the BDS value, calculated using M_{rs}/M_s and B_{cr}/B_c data. Thermal changes in k or hysteresis parameters and differences between the heating and cooling curves from the thermomagnetic analysis can indicate the thermal stability of magnetic carriers in a specimen. These investigations have primarily been performed together with applying Thellier-type API determination. Unfortunately, no quantitative relationship between the proxies of rock-magnetic properties and API results has been well established as a determinative preselection tool for API data fidelity.

Over the past two decades, applications of the Tsunakawa–Shaw (TS) API method have gradually increased. The TS method is the most advanced version of the Shaw method (Shaw 1974). It determines an API in the coercivity space by performing progressive altering field (AF) demagnetization (AFD) for each of the natural remanent magnetization and laboratory-induced remanent magnetizations of a specimen, with the implementation of anhysteretic remanent magnetization (ARM) correction (Rolph and Shaw 1985), double heating test (Tsunakawa and Shaw 1994), and low-temperature demagnetization
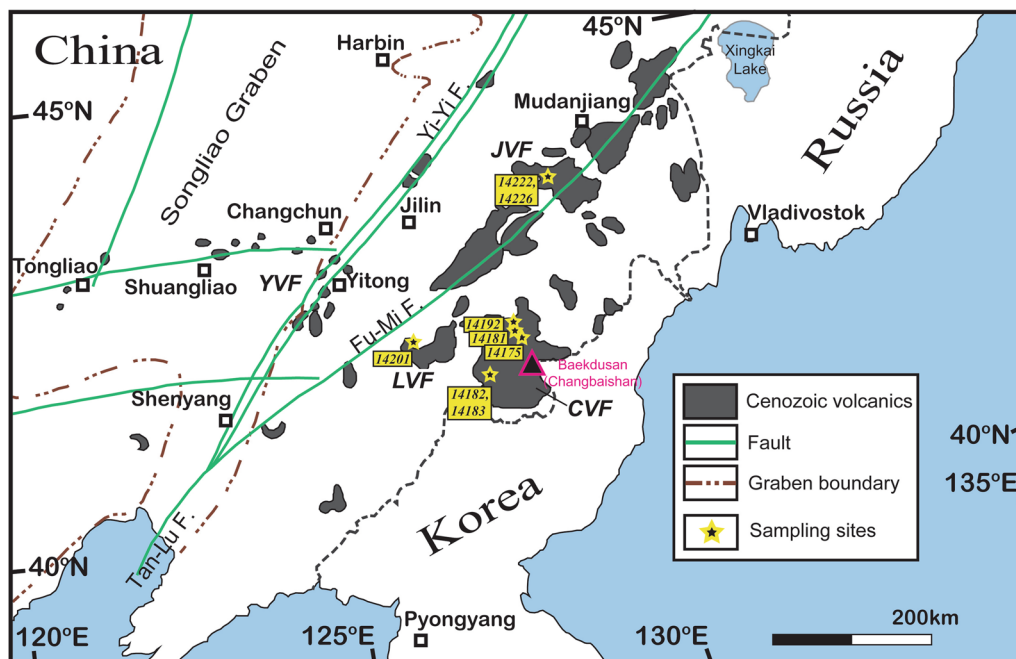
Fig. 1 Schematic map showing the distribution of Cenozoic volcanics in Northeast (NE) China and locations of sampling sites of Cenozoic basalt rocks. The sampling campaign was conducted through a 2014–2016 Korean-Chinese cooperative project of Baekdusan (Changbaishan) volcano. Distributions of the volcanic rocks, faults, and graben boundaries are from Liu et al. (2001). *CVF* Changbaishan volcanic field, *LVF* Longgang volcanic field, *JVF* Jingbohu volcanic field, *YVF* Yitong volcanic field, *Tan-Lu F.* Tan-Lu fault, *Fu-Mi F.* Fushun-Mishan fault, *Yi-Yi F.* Yitong-Yilan fault

Ahn *et al. Earth, Planets and Space*   (2024) 76:9

Page 4 of 29

Table 1 Brief information on the sampled sites and associated age constraints of the Northeast (NE) China volcanic field analyzed in this study

Site name	Name of basalt/volcanic field	Sampling locality			Age info
		Area name	Lat. (° N)	Lon. (° E)	
14175	Naitoushan Basalt/CVF	Naitoushan	42.33219	128.14203	Miocene (Liu 1983, 1987, 1988; Chun and Cheong 2020)
14192	Toudao Basalt/CVF	Yaoshui	42.52450	128.05640	~2.8~1.9 Ma (Wei et al. 2007), ~2.5 Ma (sample B5102 of the same outcrop in Lee et al. 2021)
14181	Toudao Basalt/CVF	Baomacun	42.41610	128.04347	same as those of site 14192
14182	Toudao Basalt/CVF	Jinjiangcun	41.97798	127.55910	same as those of site 14192 (the same site as where the sample B4182 was collected in Lee et al. 2021)
14183	Baishan Basalt/CVF	Jinjiangcun	41.98098	127.56295	~1.4~0.9 Ma (Wei et al. 2007), ~1.1 Ma (the Baishan Basalt sample B5104 in Lee et al. 2021)
14201	Longgang Basalt/LVF	Longgang	42.49373	126.47533	~1.2 Ma (basanite at Dalongwan area in Liu 1987), ~0.9 Ma (unpublished direct K–Ar data, credit by Dr. Y. S. Lee)
14222	Jingpohu Basalt/JVF	Jingpohu	44.07695	128.99215	Late Pleistocene to Holocene around Xingshan area (Liu et al. 1989; Yan and Zhao 2008), ~0.12 Ma (unpublished direct K–Ar data, credit by Dr. Y. S. Lee)
14226	Jingpohu Basalt/JVF	Jingpohu	44.06550	128.94912	Late Pleistocene to Holocene (Liu et al. 1989; Yan and Zhao 2008), ~0.08 Ma (unpublished direct K–Ar data, credit by Dr. Y. S. Lee)

CVF, LVF, and JVF represent the Changbaishan (Baekdusan), Longgang, and Jingpohu volcanic fields, respectively

before each progressive AFD (Yamamoto et al. 2003). It has achieved successful determinations in historical lava rocks, burnt archeological materials, and geologically ancient volcanic and granitic rocks, even with nonideal magnetic behaviors (non-single-domain-dominated) (Yamamoto et al. 2003; Mochizuki et al. 2004, 2006, 2011, 2013, 2021; Oishi et al. 2005; Yamamoto and Tsunakawa 2005; Yamamoto and Hoshi 2008; Tsunakawa et al. 2009; Ahn et al. 2016; Kato et al. 2018; Kitahara et al. 2018, 2021; Yamamoto and Yamaoka 2018; Ahn and Yamamoto 2019; Okayama et al. 2019; Singer et al. 2019; Yoshimura et al. 2020; Lloyd et al. 2021), and in materials with artificially laboratory-aged TRM (Yamamoto et al. 2022). Empirically, in these TS API determinations for NRMs of historical volcanic rocks and laboratory-aged TRMs, no significant determination bias due to cooling rate effects has been identified. For the applicability and usability of the TS method, exploring and evaluating potential links between the API results and rock-magnetic properties retrieved from separate rapid measurements is required for time-saving in laborious experiments and enhancing API data fidelity.

These TS API studies have provided data on rock-magnetic properties such as strong-field high-temperature thermomagnetic (M_s-T) curves and hysteresis data (Yamamoto et al. 2003, 2015; Mochizuki et al. 2004, 2006, 2011, 2013; Yamamoto and Tsunakawa 2005; Ahn et al. 2016; Kitahara et al. 2018, 2021; Yamamoto and Yamaoka 2018; Ahn and Yamamoto 2019; Yoshimura et al. 2020). Notably, thermomagnetic curve data were previously used to roughly assess the thermal stability

of magnetization by visual inspection, identify magnetic minerals as remanence carriers, and detect the occurrence of hump-shaped behaviors in the heating curve. The "hump" can indicate the presence of titanomaghemite, which is a low-temperature by-product after the initial emplacement of volcanic rock bodies (Grommé et al. 1969; Marshall and Cox 1971; Özdemir and Dunlop 1985) and is suspected to cause unwanted effects by acquisition of chemical remanence that replaces or overprints the primary TRM, i.e., failure in or erroneous API determination (Yamamoto and Tsunakawa 2005; Gee et al. 2010; Paterson et al. 2010). However, quantifying rock-magnetic properties, particularly the thermal stability from thermomagnetic curves, and ascertaining its association with TS API results require further investigation.

This study explored the quantifiable relationships between (rapidly obtainable) rock-magnetic parameters and TS API results, and criteria with rock-magnetic parameters for efficient sample preselection using in the TS method. First, we conducted rock-magnetic experiments and API determinations by the TS method on late Cenozoic basalt samples from Northeast (NE) China volcanic fields. We present new paired data from the TS API, M_s-T curves, and magnetic hysteresis experiments. Second, we compiled a large-volume dataset from new and previously published data of the same quality for late Cenozoic basalts bearing titanomagnetite. Here, we use BDS, M_{rs}/M_s, B_{cr}/B_c, B_{cr}, and B_c data, and parameter data quantified from thermomagnetic curves, that is, ITC_{50} and $ITC_{|m|}$ ("Ms-T curves and ITC parameters" section),

Ahn *et al. Earth, Planets and Space*   (2024) 76:9

Page 5 of 29

which are measures of thermally induced magnetic change during a heating–cooling cycle (thermal stability). These parameters are called 'ease-of-use' rock-magnetic parameters. Using the compiled dataset, we found meaningful relationships between the rock-magnetic parameters and individual acceptance (success or failure) of the associated TS API estimates. These relationships represent a guideline for effective, time-saving sample preselection before the API experiment and high fidelity of the API estimate after the API experiment using the TS method.

Materials

Cenozoic basalts of NE China volcanic fields

There are several Cenozoic volcanic fields (Changbaishan volcanic field [CVF], Longgang volcanic field [LVF], Jingpohu volcanic field [JVF], and Yitong volcanic field; Fig. 1) in NE China where basaltic products (calc-alkaline and alkali basalts) are widely distributed between the Late Cretaceous and Late Quaternary, mainly concentrated in the Miocene and Quaternary (Wang et al. 1988; Liu 1987; Liu et al. 2001; Wei et al. 2013). We sampled 56 oriented block samples of basaltic rocks from 8 sites (≈cooling units) in the CVF, LVF, and JVF (Fig. 1); the sampling was conducted through a 2014–2016 Korean-Chinese cooperative research project studying the Baekdusan (Changbaishan) volcano and its surrounding volcanic fields. Sites 14175, 14192, 14181, 14182, and 14183 belong to the CVF, site 14201 belongs to the LVF, and sites 14222 and 14226 belong to the JVF. Brief information on the sampling sites and associated age constraints is summarized in Table 1.

Several oriented cylindrical specimens and several nonoriented tiny fragment specimens were prepared from each of the collected block samples and used to determine paleomagnetic directions, API estimates, M_sT curves, and measurements of the magnetic hysteresis parameters. The context regarding paleomagnetic directions is briefly addressed in this study ("API determination results" section) because of minimal interest.

Cenozoic basalts with previously published data

This study used previously published data (TS API and rock-magnetic data) for the late Cenozoic basalts of the Ethiopian Afar and Baengnyeong Island (South Korea) from Ahn et al. (2016) and Ahn and Yamamoto (2019), respectively. The geological background and samples from these two areas are briefly introduced.

Many piles of basaltic lavas with Plio-Pleistocene ages are found in the Afar Depression, which lies at the East African triple junction of the Red Sea, Gulf of Aden, and Ethiopian rifts. Geologically recent tectonic activities have exposed thick sequences of basaltic lava piles

along high cliffs formed by normal faulting. Ahn et al. (2016) introduced good exposures of a thick basaltic lava sequence ~ 350 m tall along high cliffs in the Dobi area, Ethiopian Afar (11.84°N, 41.67°E) and collected 112 oriented block samples from 29 successive lava flows (each likely corresponding to a cooling unit) for paleomagnetic investigation. The ages of the collected basaltic samples were estimated to be in the early Matuyama reversed chron, covering the early Olduvai normal subchron, ~ 2.4–1.9 Ma.

Baengnyeong Island (37.92°N, 124.67°E; 45 km^2), the subject region of Ahn and Yamamoto (2019), is located off the furthest northwest point of South Korea. Most of the island surface is occupied by Proterozoic metasedimentary rocks (slate, phyllite, and quartzite), and in the northeastern part of the island, covering ~ 4 km^2, intrusive and extrusive basaltic rocks called the Jinchon Basalt are exposed, which is the subject of the paleomagnetic study. The Jinchon Basalt rocks are products of late Cenozoic alkali magmatism, likely caused by dramatic changes in stress regimes under the interplay between the India and Eurasia collision and the subduction of the Pacific Plate beneath the eastern margin of Eurasia (Choi et al. 2006). Ahn and Yamamoto (2019) collected seven oriented block samples from each of two exposure sites (B1 and B2) along the northeast coast for paleomagnetic investigation. The ages of the samples were in the Early Pliocene, at approximately 4–5 Ma.

Methods

NE China basalts

Magnetic hysteresis parameters, BDS, and first-order reversal curves (FORCs)

The hysteresis parameter data were acquired from the hysteresis loop and back-field measurements with a tiny fragment of tens of milligrams at room temperature in ambient air using a Princeton Measurements Corporation (PMC) MicroMag 3900 Vibrating Sample Magnetometer (VSM) at the Korea Institute of Geoscience and Mineral Resources (KIGAM). Each hysteresis loop was measured by applying magnetic fields up to 1.0 T, and the measured data were corrected for paramagnetic and diamagnetic contributions using a high-field slope correction. This enabled the determination of M_s, M_{rs}, and B_c. B_{cr} was determined from the back-field demagnetization of the saturation remanent magnetization. Then, the hysteresis ratio combinations M_{rs}/M_s and B_{cr}/B_c were calculated. The hysteresis ratio combinations were used to calculate the BDS value as follows (Paterson et al. 2017):

$$BDS = -0.3900 \left\{ \log_{10}(X) - 0.6062 \right\} \\ + 0.6353 \left\{ \log_{10}(Y) + 1.2018 \right\}$$

Ahn *et al. Earth, Planets and Space* (2024) 76:9

Page 6 of 29

where X represents B_{cr}/B_c data and Y represents M_{rs}/M_s data. All the acquired data are provided in Additional file 1: Table S1. The B_{cr}, B_c, B_{cr}/B_c, M_{rs}/M_s, and BDS values were used to explore possible relationships with the TS API results. These hysteresis parameters are associated with an effective bulk magnetic domain state that may control the thermal change of remanence capacity, thus, "BDS" (Paterson et al. 2017).

For a limited number of samples, FORC diagrams were constructed at room temperature, processing data with FORCinel (Harrison and Feinberg 2008) to more definitively diagnose the magnetic domain states (Roberts et al. 2014, 2018b). The measurement and processing parameters are provided in Additional file 2: Figure S1.

M$_s$-T curves and ITC parameters

Thermomagnetic curve data were acquired from M_s-T analysis with a tiny fragment of tens of milligrams in a vacuum environment (1–10 Pa) using a Natsuhara Giken NMB-89 magnetic balance at the Marine Core Research Institute (MaCRI), Kochi University. During analysis, the specimen was heated from ~20 to 580 °C (or 610 °C or 700 °C) and then cooled to 50 °C, with an average heating/cooling rate of ~15 °C/min in a constant applied field of 0.3 T (or 0.5 T). The running time for a single cycle was ~1.5 h. The measured thermomagnetic curve data, displaying temperature variation in saturation magnetization (M_s vs. T) during the heating–cooling cycle, were reprocessed by a spline smoothing fitting to each of the heating and cooling run data to place data points at every 1 °C interval between 50 °C and 580 °C (or 610 °C or 700 °C).

Two different indices of thermal change, herein called ITC_{50} and $ITC_{|m|}$, were prepared to quantify the change in M_s after the heating–cooling run using the reprocessed data. The ITC_{50} value was calculated as follows:

$$ITC_{50} = (m_{50} - M_{50})/M_{50}$$

where m_{50} and M_{50} are the induced current values in proportional response to the M_s values on the cooling and heating curves at 50 °C, respectively. The $ITC_{|m|}$ value is given by:

$$ITC_{|m|} = \sum_{i=1}^{N} |(m_i - M_i)|/(NM_{50})$$

where m_i and M_i are the values corresponding to the induced saturation magnetizations on the cooling and heating curves at the same i-th temperature, which ranges from 50 to 580 °C (or 610 °C or 700 °C) at 1 °C intervals; N is the number of the total data pairs of the feedback current values, proportional to the strong-field magnetization; and M_{50} is the current (induced saturation magnetization) value on the heating curve at 50 °C.

These indices were designed similar to the alteration indices introduced by Hrouda et al. (2002) and Hrouda (2003). The calculated ITC data are presented in Additional file 1: Table S1 and were used to explore the relationships with the TS API results.

API determination

All API experiments were performed at the MaCRI, Kochi University.

For cylindrical specimens cored from basaltic rock samples, all of which had associated hysteresis and thermomagnetic curve data, each API experiment using the TS method was conducted following a procedure similar to that of most TS-based paleointensity studies (Ahn and Yamamoto 2019). Remanence measurements, AFD treatments, and ARM acquisition were performed using a DSPIN automated system (Natsuhara Giken). AFD treatments were performed with 38 (or 34) steps in the peak AFs from 2 to 180 (or 140) mT. Three ARMs for each specimen were imparted by a direct current (DC) bias field of 50 µT with peak AFs of 180 mT, in which the bias field directions were (sub-)parallel to the characteristic directions of NRM or the laboratory-induced TRM directions. To impart the laboratory TRMs, the specimens were heated to 580 °C in a vacuum (mostly < 50 Pa), maintained for 15 min (for the first TRM acquisition, TRM1) and 60 min (for the second TRM acquisition, TRM2), and then cooled to room temperature for ~3 h, using a TDS-1 thermal demagnetizer with a built-in DC field coil (Natsuhara Giken). The DC field was mainly set to 50 µT (occasionally 10, 25, or 30 µT). A low-temperature demagnetization was conducted before starting the progressive AFD treatment of the remanent magnetization.

The TS API experimental result per specimen was evaluated using a minimal set of the following determination criteria [similar to those described in Ahn and Yamamoto (2019)], and an API value was estimated by determining the slope of the linear segment defined for the NRM-TRM1* diagram when the ARM correction was validated by the unity slope of the linear segment of the TRM1–TRM2* diagram:

1. A primary NRM component should be isolated by progressive AFD on the Zijderveld diagram (anchored $MAD_{anc} < 10°$, where MAD represents the maximum angular deviation; that is, a measure of precision when the best-fit line for the selected component is determined).
2. On the NRM-ARM1* diagram, a single linear segment for slope calculation should be recognized within the coercivity range defining the primary NRM component. The segment should have at least

Ahn *et al. Earth, Planets and Space* (2024) 76:9

Page 7 of 29

30% in NRM fraction [we used the statistic FRAC suggested by Shaar and Tauxe (2013)]: $FRAC_N \geq 0.30$; the earlier TS API determinations of Ahn et al. (2016) used the NRM fraction statistic equivalent to that designed by Coe et al. (1978). The associated correlation coefficient should not be < 0.995 ($r_N \geq 0.995$).

3. On the TRM1-TRM2* diagram, a single linear segment should be recognized with $FRAC_T \geq 0.30$ and $r_T \geq 0.995$. The linear segment slope is unity within experimental errors with $1.05 \geq slope_T \geq 0.95$ to validate the ARM correction.

No criterion based on other independent measurements, such as hysteresis measurements and thermomagnetic analyses, was included at this level of acceptance evaluation, later referred to as 'success' or 'failure'. The determined specimen-level API values were used in consideration of sample- and site-level API determinations, which discuss their relationships with rock-magnetic parameters.

Additionally, only a minimal set of cylindrical specimens (retrieved from eight block samples from three sites: 14181-B, 14181-E, 14181-F, 14181-G, 14222-B, 14222-D, 14226-C, and 14226-E) were subjected to Thellier-type API experiment by applying the experimental protocol of Coe et al. (1967) (also called 'Coe-Thellier" API experiment/method/protocol), for comparison with correlating TS API estimates. However, because these Coe-Thellier API experiments and results were not of major interest, descriptions of the method and results have been restricted to Additional file 3: Additional information note.

Preparing previously published data and an extended data compilation

In addition to the new NE China basalt data, we collected previously published specimen level, magnetic hysteresis, M_s-T curve, and TS API data for late Cenozoic basalts from Ahn et al. (2016) (Ethiopian Afar) and Ahn and Yamamoto (2019) (Baengnyeong Island) to use a larger amount of data in analyses. All measurements, including the magnetic hysteresis parameters (and BDS), M_s-T curves, and TS API determinations for the previously published data, were conducted at MaCRI, Kochi University. The individual experimental procedures were similar to those for the NE China basalts, as summarized below.

The magnetic hysteresis parameters (and BDS) for the previously published data were measured using a PMC MicroMag 3900 VSM with set operational values similar to those for NE China basalts. Only the maximum applied field varied: 1.8 T and 0.5 T for the Ethiopian

Afar and Baengnyeong Island basalts, respectively. The determination of M_s, M_{rs}, B_c, and B_{cr} and the calculation of BDS were the same as those for the NE China basalts. The hysteresis data were generally measured once for each block sample, except for a few in which up to four specimens were measured per sample.

All M_s-T curve measurements for the previous data were performed using a Natsuhara Giken NMB-89 magnetic balance identical to that used for the NE China basalts. The M_s-T curves for the Ethiopian Afar were obtained by heating to 700 °C with an average heat rate of ~ 10 °C/min in a constant DC field of 0.5 T under a vacuum (1–10 Pa). The M_s-T curves for the Baengnyeong Island basalts were obtained under almost the same experimental conditions but under ambient air. The data processing and calculations for ITC_{50} and $ITC_{|m|}$ from each of the M_s-T curves were the same as those for the NE China basalts. An M_s-T curve per block sample was obtained. However, the curve data from the block samples revealing the 'hump-shaped' behavior during heating ("Type U" of M_s-T curve behavior category in Ahn et al. 2016; 15 samples) were excluded because of the presence of titanomaghemite.

Most TS API determination experiments for the previous data were performed with the same instruments and almost identical conditions to those for the NE China basalts; one differing condition was the maximum heat temperature in the TRM acquisitions, which was set to 610 °C. On the other hand, only four of the Ethiopian Afar TS experiments were performed using a Natsuhara Giken SMD-88 spinner magnetometer and Natsuhara Giken DEM-8601C AF demagnetizer equipped with a coil for ARM acquisition for remanence measurements and demagnetizations. In these cases, each progressive demagnetization comprised 17 AF steps up to 140 mT. A total of 127 specimen-level TS experimental data (belonging to 30 sites) were individually evaluated using the same criteria for specimen-level API determination acceptance as those for the NE China basalts. Our analyses adopted previous acceptance interpretations and API estimates (where accepted) at the specimen level.

Due to the occasional presence of multiple specimen-level data for a single sample, we prepared a 'sample-level' data compilation comprising the hysteresis, M_s-T, and TS API data from the new and previous 'specimen-level' data. Multiple specimen-level data points for a single sample were averaged to obtain the sample-level data for the given sample. Only three sample-level data pairs could be prepared for samples from sites B1 and B2 in Ahn and Yamamoto (2019) because of the loss of M_s-T measurement data.
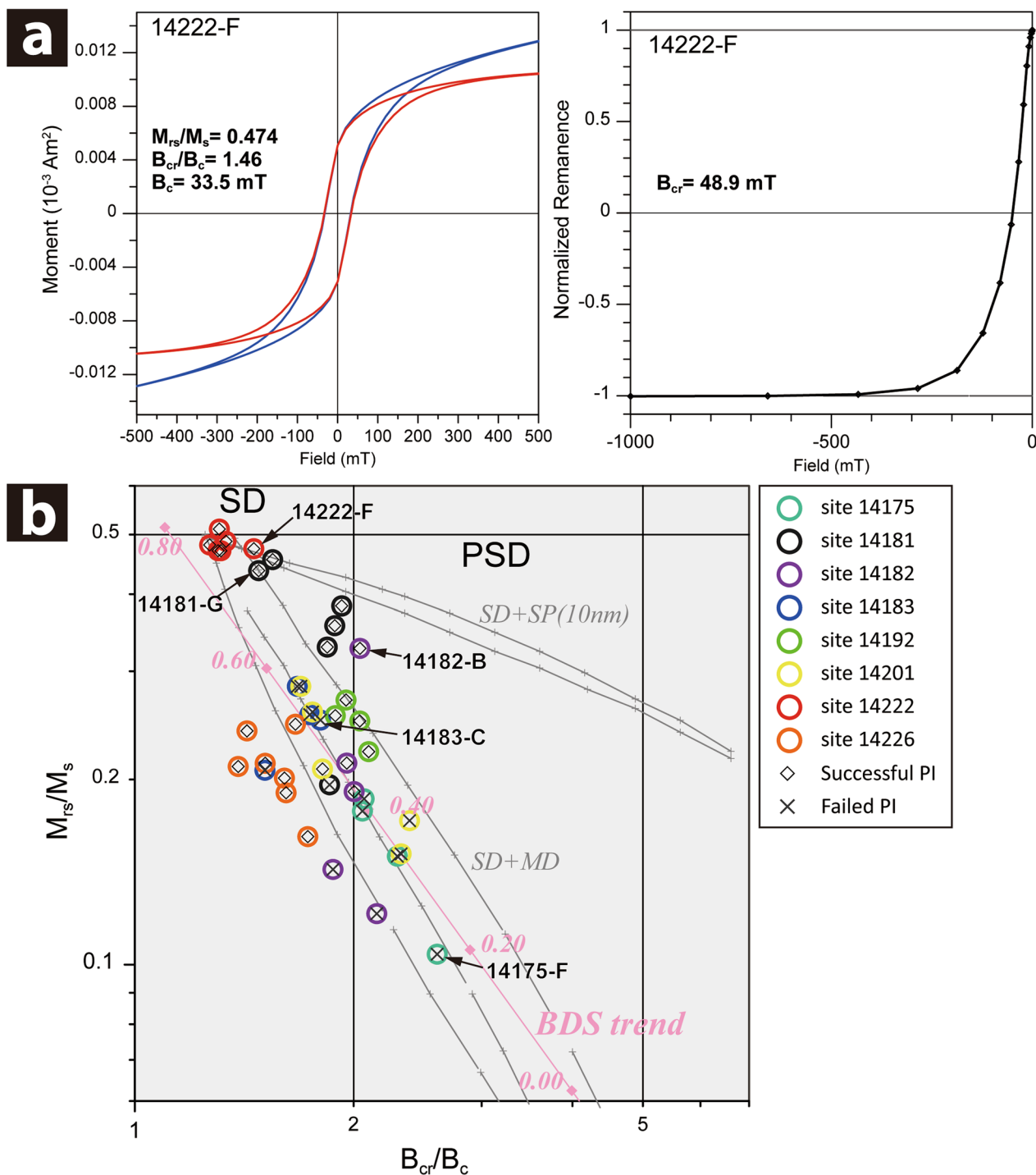
Fig. 2 Summary of results of the magnetic hysteresis properties from Vibrating Sample Magnetometer measurements of the NE China basalts. **a** Hysteresis loops (raw and corrected) and back-field curve for a representative sample (14222-F). The determined B_c, B_{cr}, B_{cr}/B_c, and M_{rs}/M_s values are given. **b** Biplot of M_{rs}/M_s vs. B_{cr}/B_c (the so-called Day plot) in logarithmic space for the NE China basalt samples. Each circle symbol corresponds to the result from each block sample. The circles with the same color represent the results of samples from the same site. The diamond or cross symbol inscribed in each circle symbol indicates the "success" or "failure" Tsunakawa–Shaw (TS) absolute paleomagnetic field intensity (API) determination (Table 3), respectively. The theoretical curves for the mixtures of single-domain (SD) and multi-domain (MD) particles (three gray long-dashed lines) and SD and SP (10 nm in size) particles (two gray solid lines). The boundaries for the SD and pseudo-SD (PSD) regions suggested by Dunlop (2002a, b), and the bulk domain stability (BDS) trend line (pink solid line) with labels of some BDS values (diamond symbols) suggested by Paterson et al. (2017) are also shown. For the five data points with the sample labeling, the corresponding First-order reversal curve diagrams are provided in Additional file 2: Figure S1

Ahn *et al. Earth, Planets and Space*   (2024) 76:9

Page 9 of 29

Table 2 Summary of statistics of individual rock-magnetic parameters obtained in the NE China basalt samples

	B_{cr}	B_c	B_{cr}/B_c	M_{rs}/M_s	BDS	$|ITC_{50}|$	$ITC_{|m|}$
n	41	41	41	41	41	41	41
Min	11.74	5.47	1.267	0.104	0.213	0.016	0.013
Max	79.05	51.09	2.606	0.510	0.769	3.172	1.212
Mean	31.21	18.22	1.785	0.273	0.523	0.357	0.187
Median	22.81	12.54	1.801	0.246	0.514	0.152	0.120
Q1	15.05	8.96	1.511	0.191	0.441	0.086	0.080
Q3	47.42	27.53	2.012	0.335	0.594	0.417	0.260
Std	18.77	11.65	0.325	0.116	0.138	0.539	0.199

n number of sample-level data, *Min. and Max.* minimum and maximum values, respectively, *Q1 and Q3* first and third quartile values, respectively, *Std.* standard deviation

Results

New data from NE China basalts

Rock-magnetic results

Forty-one tiny specimens (one specimen per sample) underwent hysteresis loop and back-field-curve measurements. Figure 2a shows hysteresis loops, back-field curves, and the determined B_c, B_{cr}, B_{cr}/B_c, and M_{rs}/M_s values. These specimen-level values were considered equivalent to the sample-level values. B_c, B_{cr}, B_{cr}/B_c, M_{rs}/M_s, and associated BDS values ranged from 5.5–51 mT, 12–79 mT, 1.3–2.6, 0.10–0.51, and 0.21–0.77, respectively; the data and their fundamental statistics are presented in Additional file 1: Table S1 and Table 2, respectively. A biplot of the hysteresis combination ratios, B_{cr}/B_c and M_{rs}/M_s ('Day plot;' Day et al. 1977), for 41 data and the BDS trend line (Paterson et al. 2017) are shown in Fig. 2b. In the Day plot, the data are plotted in the single-domain (SD) region, pseudo-SD (PSD) region, or the left-side region outside the PSD region; the majority are also aligned along or near the SD + multi-domain (MD) mixing lines, as suggested by Dunlop (2002a, b). The data distribution within a site is well-clustered or dispersed, differing between sites. In addition to the Day plot results, FORC diagrams were generated for samples 14175-F, 14181-G, 14182-B, 14183-C, and 14222-F (Additional file 2: Figure S1). The FORC diagrams of samples 14222-F and 14181-G indicated an SD-like behavior consistent with the interpretation of the bulk domain state using the Day plot. The PSD behavior in the Day plot for sample 14182-B can be attributed to a mixture of SD and vortex (PSD)/MD particles. Sample 14183-C, indicating PSD or SD + MD mixing by the Day plot results, represents the predominance of fine vortex particles in the FORC diagram. The FORC diagram of sample 14175-F indicates coarse vortex/MD particles, whereas the associated Day plot result suggests a PSD or SD + MD mixing behavior.

Forty-four tiny specimens (generally one specimen per sample, except for three samples) underwent M_s-T analysis (under a vacuum). Figure 3 shows the heating–cooling curves for the 15 sample examples. The heating curves showed a predominant magnetic mineral phase(s) with variable Curie temperatures (T_cs; ~ 100 °C to 580 °C) from sample to sample, presumably associated with titano-magnetite with variable degrees of Ti substitution. Based on the T_c of the predominant mineral phase, the analyzed samples can be classified into Category I, with ≥ 400 °C in T_c of the predominant phase (107 in total), and Category II, which involves the others (26 in total) (Additional file 4: Table S2). ITC_{50} and $ITC_{|m|}$ were calculated for each M_s-T curve (Fig. 3). Each specimen-level value was regarded as its sample-level representative value; however, for three samples, two were averaged as a sample-level value. These resultant sample-level ITC_{50} and $ITC_{|m|}$ values ranged from near zero–3.2 and near zero–1.2, respectively. The absolute ITC_{50}s (hereafter, $|ITC_{50}|$) and $ITC_{|m|}$ values were used to explore the relationships with the paleointensity results ("Results from the extended data compilation" section). The sample-level indices and individual fundamental statistics are listed in Additional file 1: Table S1 and Table 2, respectively.

API determination results

Before describing the API experimental results, we briefly introduce the results of the NRM demagnetization behavior obtained from the NRM AFD step in the Tsunakawa−Shaw (TS) experiments. The results of one representative specimen from each site are shown in Additional file 5: Figure S2. Each demagnetization result generally displayed one or two directional remanence components. The low AF level (secondary) remanence component was removed by the pre-treatment with low-temperature demagnetization and/or by up to 4–26 mT AF. Generally, it represented a small portion of the total

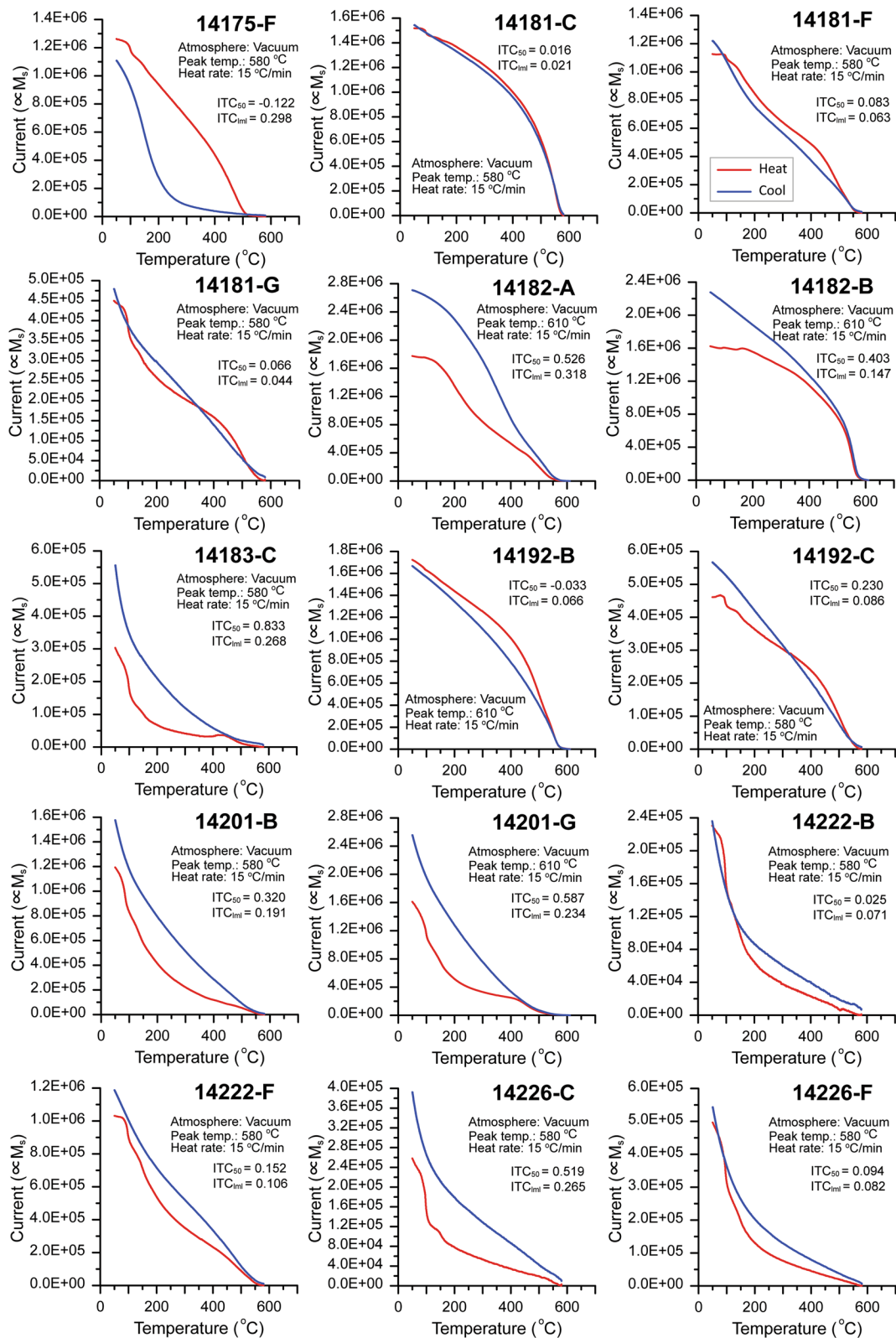**Fig. 3** Examples of strong-field high-temperature curves (M_s-T curves) between the room temperature and 700 °C. Red and blue lines for each result indicate heating and cooling curves, respectively. The indices of thermal change, ITC_{50} and $ITC_{|m|}$, are also given

Ahn *et al. Earth, Planets and Space* (2024) 76:9

Page 11 of 29

NRM. However, the specimens from sites 14175, 14182, and 14201 showed a relatively large proportion of the low AF level component. Furthermore, a few specimens encountered difficulty in characteristic remanent magnetization (ChRM) isolation owing to a strong overlap of the two remanence components (not shown), particularly at site 14201. The high-AF level remanence component for most specimens was well defined (i.e., small MAD values) and directed toward the origin (Additional file 5: Figure S2) and was thereby considered as ChRM. The ChRM directions isolated from multiple specimens per site were similar and yielded a site-mean direction with high precision (not shown). Thus, specimen-level ChRMs are recognized individually as primary (paleomagnetic) remanence components. However, for site 14201 the ChRM directions could be grouped into two: ~190° in declination and ~−50° in inclination, and ~350° in declination and ~−55° in inclination (not shown).

Forty-two specimens underwent the TS API determination protocol. One specimen was taken from each sample, except for sample 14181-E (two specimens), and four to seven samples were collected from each site. The results for the three specimens with passed or failed API determination are shown in Fig. 4. Individual interpretations of the experimental results are summarized in Table 3. Successful specimens generally exhibited common characteristics with well-defined straight lines on the NRM-TRM1* diagrams and a uni-vector component directed to the origin on the Zijderveld orthogonal plots (Fig. 4a). Conversely, the failed specimens showed convex upward or downward and high-level interval-scattered NRM-TRM1* diagrams with or without a nonunity slope and/or convex upward TRM1-TRM2* diagrams (Fig. 4b and c). Twenty-seven specimens (~66% of the total) allowed for successful API determination, ranging from 6.3 to 66.2 µT. Three or more specimen-level API determinations were obtained from five sites (14181, 14182, 14192, 14222, and 14226), enabling them to be taken adequately for their site averages. Calculated site averages ranged from 7.4 to 61.3 µT (corresponding to 1.2×10^{22}–10.1×10^{22} Am^2 in virtual axial dipole moment), with the standard deviations ranging from 5.7 to 40.4% of the respective average (Additional file 6: Table S3).

Association between rock-magnetic parameters and API results

We briefly document several characteristics of the relationships between rock-magnetic parameters and TS API results from the NE China basalts. The NE China results likely indicate that the samples bearing SD-like particles, even those mixed with vortex/PSD particles, perform successfully in TS determination; however, those with only a vortex (PSD) or mixtures of vortex and MD particles fail. Moreover, the samples with 'intermediate' values in M_{rs}/M_s (~0.1 to 0.3) or BDS (~0.2 to 0.6) show considerable contrast in the performance of TS determinations. The site 14222 samples that involved Ti–rich titanomagnetites with SD-like behavior and good thermal stability had high success rates in specimen-level TS experiments and good within-site consistency of the TS APIs. The site 14226 samples bearing Ti–rich titanomagnetites with varying domain states and thermal alterations could allow a high success rate of specimen-level determinations and good within-site consistency. All samples from site 14175 that were thermally unstable failed to successfully determine TS API. The site 14181 samples with SD-like to coarser particles and few thermal alterations performed very well in the API determinations at the specimen level, but resulted in unwantedly scattered API values between the specimens.

Results from the extended data compilation

Our extended data compilation (made from the new NE China and two previously reported late Cenozoic basalt data) comprised 133 sample-level data pairs (acquired from the specimen-level datasets of 153 hysteresis parameter, 136 M_s-T parameter, and 168 TS API data), including B_c, B_{cr}, B_{cr}/B_c, M_{rs}/M_s, BDS, $|ITC_{50}|$, and $ITC_{|m|}$ parameter data, and TS API data with success or failure acceptance. This data compilation is suitably large; therefore, the relationships between rock-magnetic and TS API data are expected to be observable. Of the 133 data pairs, 90 (68%) represented successful TS API results. The individual sample-level parameter values and their fundamental statistics are listed in Additional file 4: Table S2 and Table 4, respectively. Using this data compilation, we compare the hysteresis and M_s-T parameters ("Comparisons between hysteresis and thermomagnetic

(See figure on next page.)
Fig. 4 Examples of specimen-level TS API results. **a** Specimen 14222-F-14 (successful in API determination), **b** Specimen 14175-F-1BL (failed in API determination), and **c** Specimen 14183-C-1A4 (failed in API determination). As the result of a single API experiment result, NRM vs. TRM1* diagram (left panel) and TRM1 vs. TRM2* diagram (right panel) are shown, where black symbols show selected data intervals for determining the linear segments (associated to API determination). Inset of a Zijderveld diagram on each NRM vs. TRM1* diagram shows the altering field demagnetization result of NRM, where filled (open) symbols indicate projection onto the horizontal (vertical) plane. Statistical values used in the API determination are also given
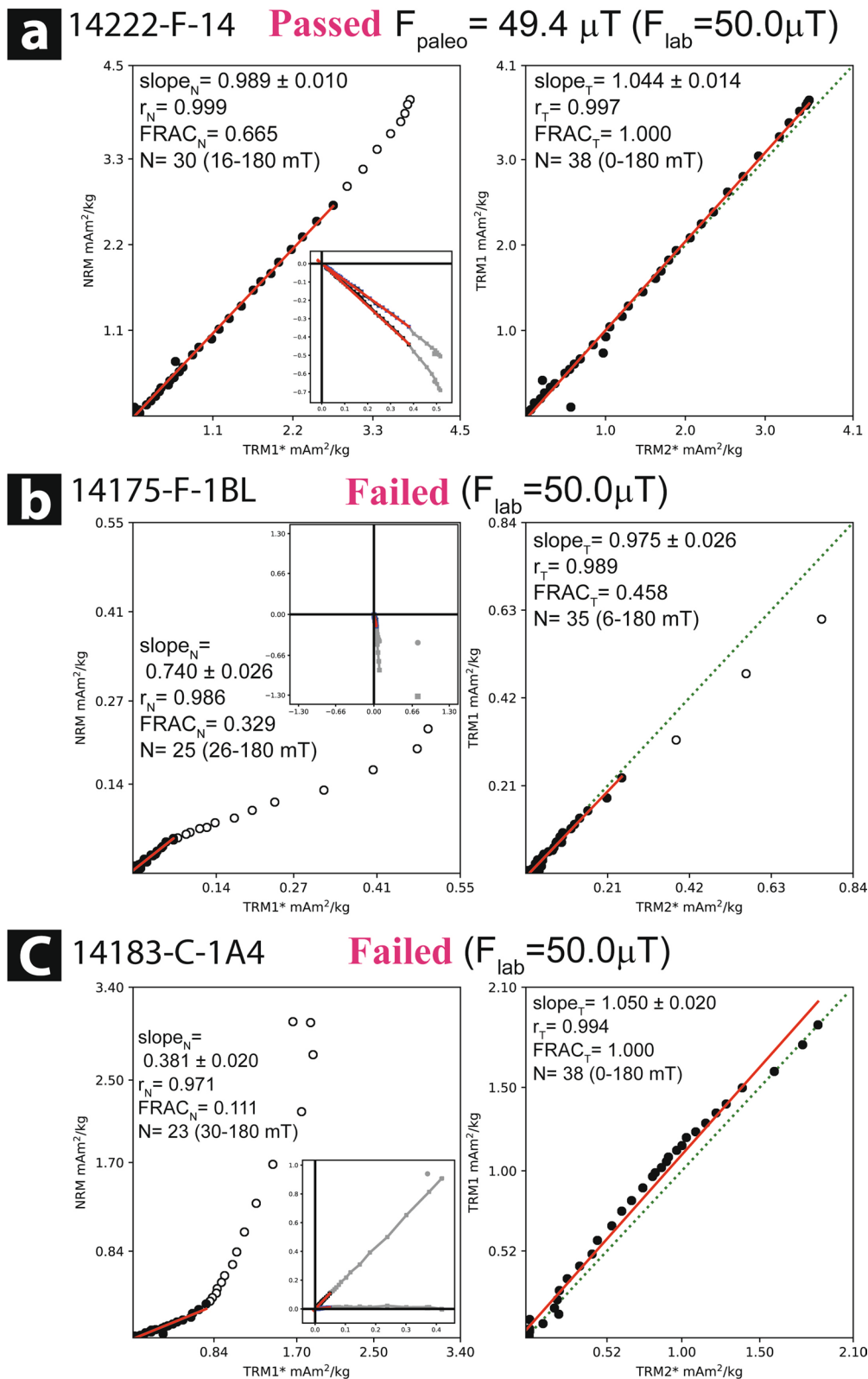
Fig. 4 (See legend on previous page.)

Table 3 Summary of specimen-level Tsunakawa–Shaw (TS) absolute paleomagnetic field intensity (API) results for the NE China basalt samples

Sample ID	$NRM_{LTD,0}$	PCA for NRM (sample-coordinate)				1st heating										2nd heating								F_{Lab}	F_{paleo}
	[Am²/kg]	Dec	Inc	MAD	N	$H_{c,1}$	$H_{c,2}$	Time	T_{MAX}	H_L	H_H	S_{NRM}	ΔS_{NRM}	$FRAC_{NRM}$	r_{NRM}	Time	T_{MAX}	H_L	H_H	S_{TRM1}	ΔS_{TRM1}	$FRAC_{TRM}$	r_{TRM}	[mT]	[mT]
14175-A-2AU	2.33E-04	75.2	32.0	3.6	27	22	180	15	580	22	180	0.675	0.035	0.497	0.968	–	–	–	–	–	–	–	–	50	*fail*
14175-B-1AU	2.28E-04	77.6	37.6	4.4	25	26	180	15	580	26	180	1.290	0.112	0.379	0.924	–	–	–	–	–	–	–	–	50	*fail*
14175-D-1AL	2.23E-04	76.4	54.4	2.9	31	14	180	15	580	14	180	0.970	0.079	0.573	0.916	30	580	0	180	1.005	0.013	1.000	0.997	50	*fail*
14175-F-1BL	2.29E-04	75.6	48.4	6.0	25	26	180	15	580	26	180	0.740	0.026	0.329	0.986	30	580	6	180	0.975	0.026	0.458	0.989	50	*fail*
14181-B-2B	2.47E-03	86.1	−14.7	1.6	38	0	180	15	580	0	180	0.662	0.009	1.000	0.997	30	580	0	180	0.935	0.003	1.000	1.000	50	*fail*
14181-C-1B14	7.40E-03	69.0	27.3	0.6	38	0	180	15	580	0	110	0.654	0.013	0.857	0.995	30	580	0	180	0.961	0.004	1.000	1.000	50	32.4
14181-D-1A4	6.58E-03	83.1	23.3	2.0	38	0	180	15	580	0	140	0.982	0.017	0.957	0.995	30	580	0	180	0.970	0.005	1.000	0.999	50	49.1
14181-E-2AL	5.49E-03	78.7	23.8	1.7	37	2	180	15	580	2	130	0.847	0.012	0.927	0.997	30	580	0	180	0.959	0.003	1.000	1.000	50	42.4
14181-E-2AU	5.50E-03	76.7	24.7	1.7	36	4	180	15	580	4	110	0.719	0.014	0.836	0.995	30	580	0	180	1.031	0.003	1.000	1.000	50	36.0
14181-F-24	3.40E-03	49.6	34.2	0.7	38	0	180	15	580	0	180	0.434	0.003	1.000	0.999	30	580	0	180	0.968	0.004	1.000	1.000	50	21.7
14181-G-1BU4	2.04E-03	94.8	−19.7	1.8	21	35	180	15	580	35	180	0.346	0.004	0.670	0.999	30	580	0	180	0.950	0.005	1.000	0.999	50	17.3
14182-A-1U	5.04E-04	83.6	52.3	6.5	30	16	180	15	610	16	180	0.307	0.014	0.347	0.974	30	610	16	180	0.958	0.013	0.716	0.998	25	*fail*
14182-B-1A1	4.86E-04	96.3	−59.5	1.9	32	12	180	15	610	12	180	0.314	0.006	0.854	0.995	30	610	4	180	0.952	0.012	0.991	0.997	25	7.9
14182-C-2A2	5.50E-04	55.5	11.1	8.3	30	16	180	15	610	16	180	0.316	0.010	0.302	0.987	30	610	16	180	0.956	0.011	0.786	0.998	25	*fail*
14182-F-1U	5.94E-04	29.0	52.9	2.9	24	20	140	15	610	20	140	0.319	0.006	0.564	0.995	30	610	20	140	0.950	0.009	0.825	0.999	25	8.0
14182-G-3A2	6.14E-04	21.3	55.7	2.2	30	16	180	15	580	16	180	0.126	0.001	0.584	0.998	30	580	0	180	0.979	0.009	1.000	0.999	50	6.3
14183-B-1B2	2.74E-03	292.6	−6.7	0.8	35	6	180	15	580	6	180	1.602	0.085	0.679	0.957	30	580	0	180	0.964	0.007	1.000	0.999	50	*fail*
14183-C-1A4	3.10E-03	294.5	−5.6	1.9	23	30	180	15	580	30	180	0.381	0.020	0.111	0.971	30	580	0	180	1.050	0.020	1.000	0.994	50	*fail*
14183-D-1A	1.45E-03	287.5	−30.4	2.2	24	28	180	15	580	28	180	0.284	0.008	0.192	0.991	30	580	0	180	*1.114*	0.025	1.000	0.991	50	*fail*
14183-G-1A1	1.84E-03	265.1	47.3	2.4	26	24	180	15	580	24	180	0.494	0.020	0.125	0.981	30	580	0	180	*1.066*	0.013	1.000	0.997	50	*fail*
14192-B-4U	1.21E-03	120.0	48.0	0.6	36	0	180	15	610	0	180	1.295	0.022	1.000	0.995	30	610	0	180	1.012	0.006	1.000	0.999	30	38.8

Table 3 (continued)

Sample ID	NRM_LTD,0 [Am²/kg]	PCA for NRM (sample-coordinate)						1st heating								2nd heating								F_Lab [mT]	F_paleo [mT]
		Dec	Inc	MAD	N	$H_{c,1}$	$H_{c,2}$	Time	T_{MAX}	H_L	H_H	S_{NRM}	ΔS_{NRM}	$FRAC_{NRM}$	r_{NRM}	Time	T_{MAX}	H_L	H_H	S_{TRM1}	ΔS_{TRM1}	$FRAC_{TRM}$	r_{TRM}		
14192-C-1A2	9.43E-04	152.0	28.6	1.0	34	8	180	15	580	8	180	0.617	0.008	0.945	0.997	30	580	0	180	0.981	0.008	1.000	0.999	50	30.9
14192-F-2U	9.93E-04	119.5	39.0	0.7	38	0	180	15	610	0	180	0.922	0.015	1.000	0.995	30	610	0	180	0.981	0.003	1.000	1.000	30	27.7
14192-G-2L	9.36E-04	77.2	7.3	0.7	38	0	180	15	610	0	180	1.375	0.013	1.000	0.998	30	610	0	180	0.984	0.007	1.000	0.999	25	34.4
14201-B-1BL	*4.48E-04*	*221.9*	*−1.4*	*3.2*	*26*	*24*	*180*	*15*	*580*	*24*	*180*	*0.146*	*0.004*	*0.290*	*0.992*	*30*	*580*	*24*	*180*	*0.913*	*0.021*	*0.482*	*0.994*	*50*	*fail*
*14201-D-1AU**	*2.35E-04*	*221.8*	*−3.8*	*4.7*	*24*	*12*	*180*	*15*	*610*	*12*	*180*	*0.424*	*0.011*	*0.388*	*0.993*	*30*	*610*	*2*	*180*	*1.003*	*0.011*	*0.971*	*0.998*	*10*	*fail*
14201-E-1AU	*2.12E-04*	*205.3*	*−2.1*	*11.5*	*27*	*22*	*180*	*15*	*610*	*22*	*180*	*0.303*	*0.016*	*0.389*	*0.965*	*30*	*610*	*8*	*180*	*0.996*	*0.018*	*0.970*	*0.995*	*10*	*fail*
14201-F-2AU	*1.96E-04*	*240.6*	*−25.4*	*7.8*	*32*	*12*	*180*	*15*	*580*	*12*	*180*	*0.119*	*0.003*	*0.441*	*0.991*	*30*	*580*	*12*	*180*	*0.800*	*0.024*	*0.748*	*0.987*	*50*	*fail*
14201-G-2U	5.33E-04	285.1	−6.8	3.5	32	12	180	15	610	12	180	0.337	0.004	0.408	0.997	30	610	2	180	0.995	0.009	0.979	0.999	25	8.4
14222-A-1A4	4.10E-03	227.0	67.0	1.6	26	24	180	15	580	24	180	1.016	0.009	0.608	0.999	30	580	16	180	1.040	0.010	0.762	0.999	50	50.8
14222-B-2A4	2.99E-03	181.7	62.6	4.3	28	20	180	15	580	20	180	1.154	0.016	0.611	0.998	30	580	2	180	1.012	0.008	0.995	0.999	50	57.7
14222-C-1BB4	4.00E-03	225.4	51.5	1.2	32	12	180	15	580	12	180	1.018	0.006	0.871	0.999	30	580	0	180	1.020	0.006	1.000	0.999	50	50.9
14222-D-2A4	5.54E-03	102.2	27.5	0.7	28	16	170	15	580	16	170	0.914	0.009	0.634	0.999	30	580	16	170	1.042	0.019	0.718	0.996	50	45.7
14222-F-14	4.19E-03	49.1	30.7	1.0	30	16	180	15	580	16	180	0.987	0.010	0.665	0.999	30	580	0	180	1.040	0.014	1.000	0.997	50	49.4
14222-G-2U4-	1.44E-03	75.0	16.5	1.3	37	0	180	15	580	0	180	1.178	0.008	1.000	0.999	30	580	0	180	0.966	0.009	1.000	0.998	50	58.9
14226-A-1AU	1.10E-03	52.6	37.0	0.9	35	6	180	15	580	6	180	1.262	0.007	0.807	0.999	30	580	0	180	1.036	0.010	1.000	0.998	50	63.1
14226-B-1BU	1.45E-03	60.2	15.6	1.0	38	4	180	15	580	4	180	1.123	0.005	0.941	1.000	30	580	0	180	0.996	0.012	1.000	0.998	50	56.2
14226-C-1BU	1.47E-03	66.1	14.2	0.8	33	8	170	15	580	8	170	1.324	0.009	0.686	0.999	30	580	0	170	0.952	0.009	1.000	0.998	50	66.2
14226-D-1BU	2.62E-03	70.0	−8.1	0.9	35	6	180	15	580	6	180	1.150	0.009	0.775	0.999	30	580	6	180	1.049	0.012	0.710	0.998	50	57.5
14226-E-1AM	2.09E-03	80.7	49.0	0.9	37	2	180	15	580	2	180	1.271	0.009	0.970	0.999	30	580	0	180	0.972	0.008	1.000	0.999	50	63.6

Ahn *et al. Earth, Planets and Space* (2024) 76:9

Page 15 of 29

Table 3 (continued)

Sample ID	NRM$_{LTD,0}$ [Am²/kg]	PCA for NRM (sample-coordinate)						1st heating								2nd heating								F$_{Lab}$ [mT]	F$_{paleo}$ [mT]
		Dec	Inc	MAD	N	H$_{c,1}$	H$_{c,2}$	Time	T$_{MAX}$	H$_L$	H$_H$	S$_{NRM}$	ΔS$_{NRM}$	FRAC$_{NRM}$	r$_{NRM}$	Time	T$_{MAX}$	H$_L$	H$_H$	S$_{TRM1}$	ΔS$_{TRM1}$	FRAC$_{TRM}$	r$_{TRM}$		
14226-F-3A1	1.72E-03	59.4	4.6	0.9	34	8	180	15	580	8	180	1.215	0.013	0.665	0.998	30	580	0	180	1.031	0.011	1.000	0.998	50	60.7
14226-G-2CU	1.72E-03	68.7	−17.1	0.7	37	2	180	15	580	2	180	1.235	0.008	0.951	0.999	30	580	0	180	1.010	0.015	1.000	0.998	50	61.8

Sample ID, specimen name used in experiment; "*" denotes the sample for which measurement artefacts occurred during altering field (AF) demagnetizations of thermo-remanence (TRM)1. NRM, TRM. NRM$_{LTD,0}$, NRM intensity after low-temperature demagnetization. In the principal component analysis (PCA) for the natural remanent magnetization (NRM; sample-coordinate) panel: Dec, Inc, and MAD, declination and inclination in the sample-coordinate system, and the maximum angular deviation determined by the PCA free-floating fit (Kirschvink 1980), respectively, for the selected data intervals; N, the number of selected data points for PCA; H$_{c,1}$ and H$_{c,2}$, the low and high limits of the interval of AF steps selected for PCA, respectively. In the 1st and 2nd heating panels: Time and T$_{MAX}$, hold time at the set peak temperature in each heating process and the set peak temperature, respectively; H$_L$ and H$_H$, low and high limits of the interval of AF steps selected for determining a linear segment; S$_N$ and S$_T$, slope values of the selected linear segment in the NRM-TRM1* and TRM1-TRM2* diagrams, respectively; FRAC$_{NRM}$ and FRAC$_{TRM}$, the NRM and TRM1 fractions of the selected linear NRM-TRM1* and TRM1-TRM2* segments, respectively; r$_N$ and r$_T$, correlation coefficients for linearity of NRM/TRM1* and TRM1/TRM2* data points in the selected linear segment, respectively. F$_{lab}$, laboratory DC fields during TRM1 and TRM2 acquisitions. F$_{paleo}$, API estimate ("fail" denotes the specimen failed in acquisition of successful API determination). "–" denotes "no data." Bold letters indicate successful API determination results. Arabic numerals in italics denote values that fail to satisfy the corresponding selection criterion ("API determination" section)

Ahn *et al. Earth, Planets and Space*   (2024) 76:9

Page 16 of 29

Table 4 Summary of statistics of the respective sample-level rock-magnetic parameters and TS API estimates in the expended data compilation

	B_{cr} (mT)	B_c (mT)	B_{cr}/B_c	M_{rs}/M_s	BDS	$|ITC_{50}|$	$ITC_{|m|}$	TS API (µT; success)	TS API (failure)
n	133	133	133	133	133	133	133	90	43
Min	8.00	3.74	1.267	0.082	0.122	0.002	0.007	3.3	–
Max	124.70	87.42	3.332	0.510	0.769	3.172	1.212	66.2	–
Mean	39.27	21.19	1.937	0.224	0.455	0.219	0.131	24.9	–
Median	36.33	18.36	1.930	0.204	0.454	0.135	0.096	19.8	–
Q1	20.99	11.24	1.732	0.161	0.365	0.064	0.066	12.0	–
Q3	52.71	27.49	2.138	0.254	0.525	0.247	0.155	32.7	–
Std	21.48	13.44	0.324	0.094	0.131	0.332	0.130	17.1	–

n number of sample-level data, *Min. and Max.* minimum and maximum values, respectively, *Q1 and Q3* first and third quartile values, respectively, *Std.* standard deviation

"-" denotes "not applicable." See "Results from the extended data compilation", and "Exploring 'ease-of-use' rock-magnetic parameters for the sample preselection criteria" sections for details

curve parameters" section) and the distributions of two data subsets for individual rock-magnetic parameters subdivided by the 'success' and 'failure' acceptance in TS API determination ("Comparisons of distributions in rock-magnetic parameter between 'successful' and 'failed' TS API data" section).

Comparisons between hysteresis and thermomagnetic curve parameters

To date, M_{rs}/M_s and BDS have been the most meaningfully addressed in the literature reporting Thellier-type API determinations with similar purposes to this study. When considering our data compilation, the success or failure in TS determination does not appear to correlate strongly with either M_{rs}/M_s or BDS (Fig. 5). This consideration will also be addressed quantitatively in "Comparisons of distributions in rock-magnetic parameter between 'successful' and 'failed' TS API data" section. This preliminary observation highlights the fundamental need to explore possible links between other rock-magnetic parameters and TS API results.

Furthermore, we must check whether the M_s-T parameters are worth considering as an alternative because these hysteresis parameters are influenced by the magnetic domain state and other factors (magnetic interactions, mineralogy, thermal fluctuations) (Paterson et al. 2017; Roberts et al. 2018a). Figure 6 shows the biplots of ITCs ($|ITC_{50}|$, $ITC_{|m|}$) vs. hysteresis parameters (B_c, B_{cr}, B_{cr}/B_c, M_{rs}/M_s, and BDS), with the correlation coefficient R and p value for each biplot. The $|ITC_{50}|$ and $ITC_{|m|}$ values had little or weak correlations with any hysteresis parameters at the 95% confidence level. This indicates that $|ITC_{50}|$ and $ITC_{|m|}$ are predominantly influenced by other major factors (potentially thermally induced magnetic changes) that differ from those acting on the hysteresis parameters.

Comparisons of distributions in rock-magnetic parameter between 'successful' and 'failed' TS API data

Figures 7 and 8 compare box plots, frequency histograms, histograms of relative frequencies in %, and cumulative distributions in relative % between the "success" and "failure" data subsets for individual hysteresis parameters and individual thermomagnetic curve parameters, respectively. Additionally, Welch's t-test was used for quantifiable comparisons between subsets. The t-statistics and p values for each parameter are listed in Table 5.

For the cases with hysteresis parameters, B_{cr}, B_c, M_{rs}/M_s, and BDS (Fig. 7a, b, d, and e) allow us to recognize differences in mean and distribution between the two "success" and "failure" data subsets through Welch's t-test at a 95% confidence level. However, B_{cr}/B_c failed to differentiate between subsets (Fig. 7c; Table 5). The differentiation is more visible in B_{cr} and B_c than in M_{rs}/M_s or BDS, displaying characteristics such as higher B_{cr}, B_c, M_{rs}/M_s, and BDS values and more successful results in TS API determination.

For the ITC cases, both $|ITC_{50}|$ and $ITC_{|m|}$ appeared to have lower values in $|ITC_{50}|$ and $ITC_{|m|}$ with more successful TS API results (Fig. 8). However, Welch's t-test results strongly suggest that only $ITC_{|m|}$ can discriminate between the 'success' and 'failure' data subsets at the 95% confidence level.

Comparison between inter-sample dispersion of API determinations and rock-magnetic parameters for sites

In paleointensity studies, multiple specimens or samples in a site/cooling unit undergo API determination; in turn, these multiple API determinations require within-site
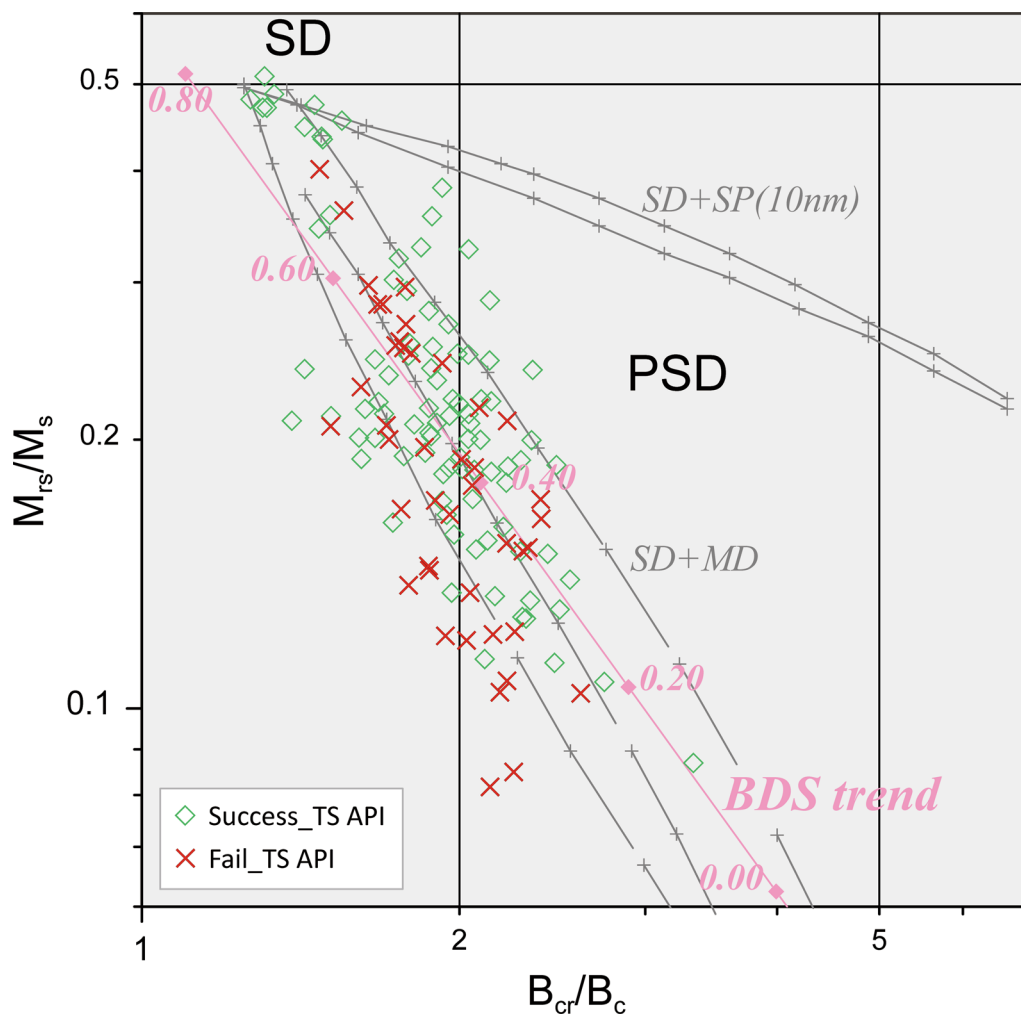
Ahn *et al. Earth, Planets and Space* (2024) 76:9

Page 17 of 29

Fig. 5 Day plot (in logarithmic space) for all data (N = 133) of the Data Compilation prepared in this study. Each circle symbol corresponds to the result from each block sample. The diamond and cross symbols indicate data with "success" and "failure" TS API determination (Table 3), respectively. The gray long-dashed lines, gray solid lines, boundary lines of x = 2, x = 5, and y = 0.5, and pink solid line with pink diamond symbols are the same as those in Fig. 2b

consistency to ensure their reliability and fidelity. However, paleomagnetists have often experienced considerable within-site dispersion of API determinations between specimens/samples, which is problematic. In our data compilation, the majority of sites with three or more specimen/sample-level TS API estimates (16 of 21 sites) had reasonably small dispersions of API estimates (< 20% in % of the standard deviation of the respective site average) (Additional file 7: Table S4). Conversely, sites 14181, DB15, DB12, DB(-1)B, and DB(-6) showed large within-site standard deviations (> 20%).

We explored the relationships between the within-site standard deviation (in % of the site average) and site average and its standard deviation (in % of the site average) for the different rock-magnetic parameters of B_c,

B_{cr}, M_{rs}/M_s, BDS, and $ITC_{|m|}$. Figure 9 shows the relationships with the correlation coefficients and p values. Most respective site averages and standard deviations of the parameters had no significant correlation with the within-site TS API standard deviations. Alternatively, the B_c standard deviations in % had a weak but statistically significant correlation with the within-site API standard deviations in % (positive correlation with $R = 0.508$ and $p = 0.026$). B_c individuals within the five sites with large within-site API standard deviations (> 20%) ranged from 12 to 51 mT (Additional file 4: Table S2), exhibiting no distribution bias.

Furthermore, as a referential comparison considering the API determination fidelity, we further explored whether the average and standard deviation (in %) of
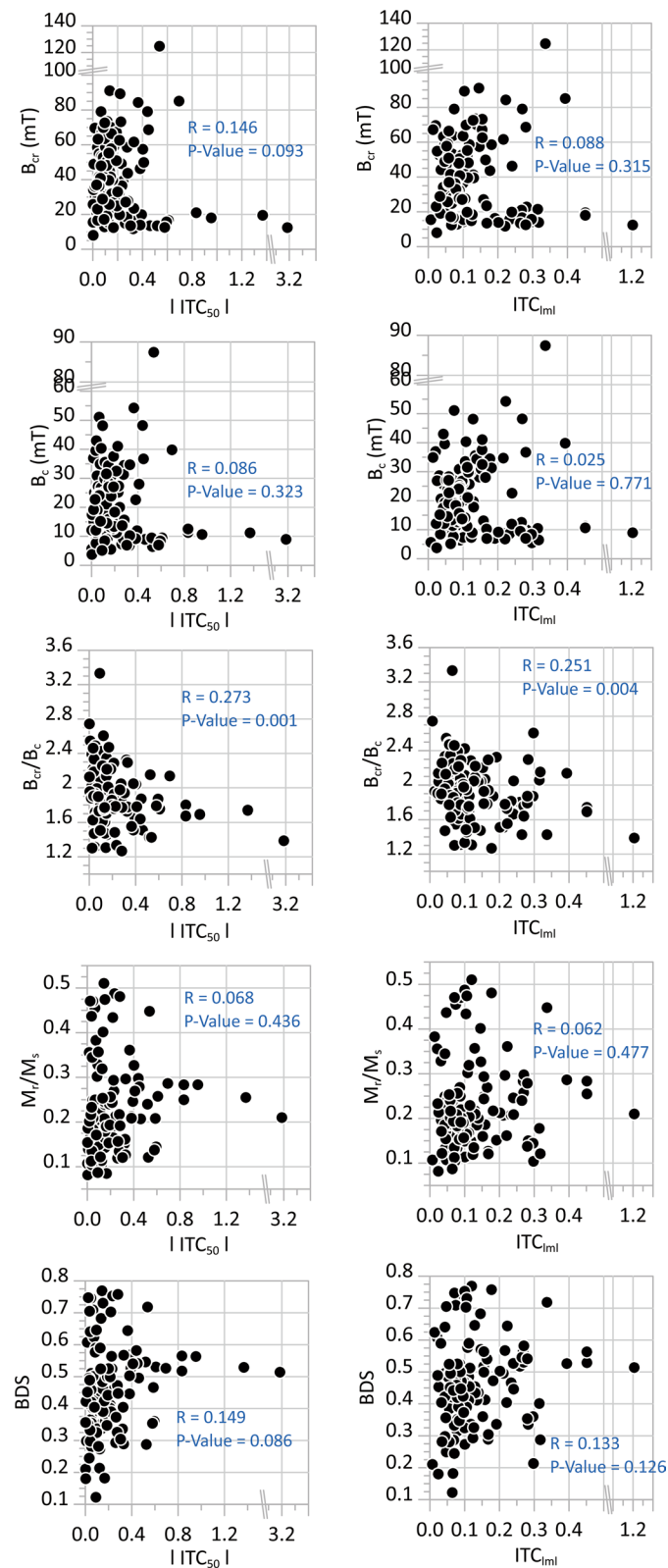
Fig. 6 Biplots of M_s-T curve parameter (ITC50, ITC|m|) vs. hysteresis parameter (B_{cr}, B_c, B_{cr}/B_c, M_{rs}/M_s, BDS) with variable combinations. Correlation coefficient value and p value for the two variables of each biplot are shown. All biplots show little or very weak correlations

Ahn *et al. Earth, Planets and Space*   (2024) 76:9

Page 19 of 29

the rock-magnetic parameters individually had no significant relationship with the TS API estimates at the site level (Fig. 10). Consequently, all the parameter statistics, except for the $ITC_{|m|}$ within-site standard deviation, indicated no meaningful correlation with the TS API site averages (low R and $p > 0.05$). The apparent (positive) correlation between the $ITC_{|m|}$ standard deviations and API site averages ($R = 0.491$ and $p = 0.038$) depended on the single data point for site 14226 with the highest $ITC_{|m|}$ standard deviation (119%) and the highest API site-average (61.3 μT) values; considering the single data exclusion, the correlations become statistically insignificant. This result rules out that our TS API estimates can be biased depending on the magnetic properties of the sample in general.

Discussion
Exploring 'ease-of-use' rock-magnetic parameters for the sample preselection criteria
'Hysteresis' parameters
Di Chiara et al. (2017) and Fukuma (2023) documented the threshold value of $M_{rs}/M_s < 0.2$ to reject, in advance, samples that potentially result in failure in Thellier-type API determination, based on their dataset from historical lava flows and scoriae, and Paleoproterozoic mafic sills, respectively. Conversely, Carvallo et al. (2006) documented that the hysteresis parameters do not appear to correlate with the success or failure of the Thellier-type API results in a large dataset for igneous rocks. Furthermore, Santos and Tauxe (2019) showed that hysteresis parameters have little relationship with the reliability of API results, although samples with higher M_{rs}/M_s tend to result in better API determinations in Thellier-type applications and vice versa. Paterson et al. (2017) introduced a BDS threshold value of 0.10 (corresponding to approximately 3.4 for B_{cr}/B_c and 0.08 for M_{rs}/M_s), where samples with a BDS < 0.10 are less likely to yield meaningful API determinations.

Let us consider the threshold values of the individual parameters for discriminating the "success" and "failure" TS results in our data compilation. The previously suggested threshold value of 0.1 in BDS cannot play a role because all BDS values are > 0.1. However, it may ensure the minimum magnetic domain stability

for the API experiments of all data compilation samples. A threshold value of 0.2 in M_{rs}/M_s allows a ~75% (54 of 72) ratio of the "success" samples to the total screened (hereafter called 'success rate') and ~40% (36 of 90) ratio of the "success" samples abandoned by the criterion to the "success" total (Fig. 11a), indicating an increasing success rate but a relatively large loss of "success" samples. When adopting 20% at maximum in the "success" samples loss rate, up to ~73% in the success rate is permitted by a threshold of 0.16 in M_{rs}/M_s (Fig. 11a). Conversely, using a threshold value in B_{cr} or B_c yields a success rate > 80% and a relatively small loss of the "success" samples (< 30%); considering 20% as the maximum "success" samples loss, we can set 26 mT in B_{cr} and 13 mT in B_c as a threshold of the minimum value (Fig. 11b and c). The highest success rate was observed for middle B_{cr} and B_c threshold values (Fig. 11b, c), which is related to the significant reduction in increasing rate in the cumulative distribution of the "failed" results (Fig. 7a, b). Consequently, B_{cr} or B_c can be used as more efficient parameters for sample preselection for TS API determination than BDS or M_{rs}/M_s.

Alternatively, FORC analysis, which has been increasingly developed in recent years, has the potential as an alternative discrimination tool for the "success" (good) or "failure" (bad) samples. The problem in BDS and M_{rs}/M_s is the considerable overlap of the two data distributions in their intermediate ranges (approximately $0.2 < BDS < 0.6$, $0.1 < M_{rs}/M_s < 0.3$). Based on our NE China cases, although it is from the limited number of data, the FORC analysis may make discernibly different domain states between samples, even with intermediate BDS or M_{rs}/M_s values ("Association between rock-magnetic parameters and API results" section). Accordingly, we encourage a future challenge using FORC analysis, as mentioned by Paterson et al. (2017).

'Thermomagnetic' parameters
As mentioned previously, the ITC parameters are likely influenced by other factors (thermal magnetic alterations associated with the change in the remanence capacity by experimental heating) that do not govern the behavior of the hysteresis parameters. Hence, this allows us to

(See figure on next page.)
Fig. 7 Comparisons of distributions in the respective hysteresis parameters, B_{cr} (**a**), B_c (**b**), B_{cr}/B_c (**c**), M_{rs}/M_s (**d**), and BDS (**e**), between the TS API "success" and "failure" data subsets. The box plot, frequency histogram, relative frequency histogram, and cumulative distribution are shown for each parameter. In the box plot, the boxes denote the interquartile ranges (IQRs), the whiskers denote the 95% ($\approx 1.5 \times$ IQR) ranges, the solid lines in the boxes are the median values, and the blue diamond symbols represent values that lie outside the 95% ranges. In the frequency histogram, distribution of the "failure" data subset is omitted for presentation clarity. For reference, distribution of all data of the Data Compilation is plotted in the frequency diagram
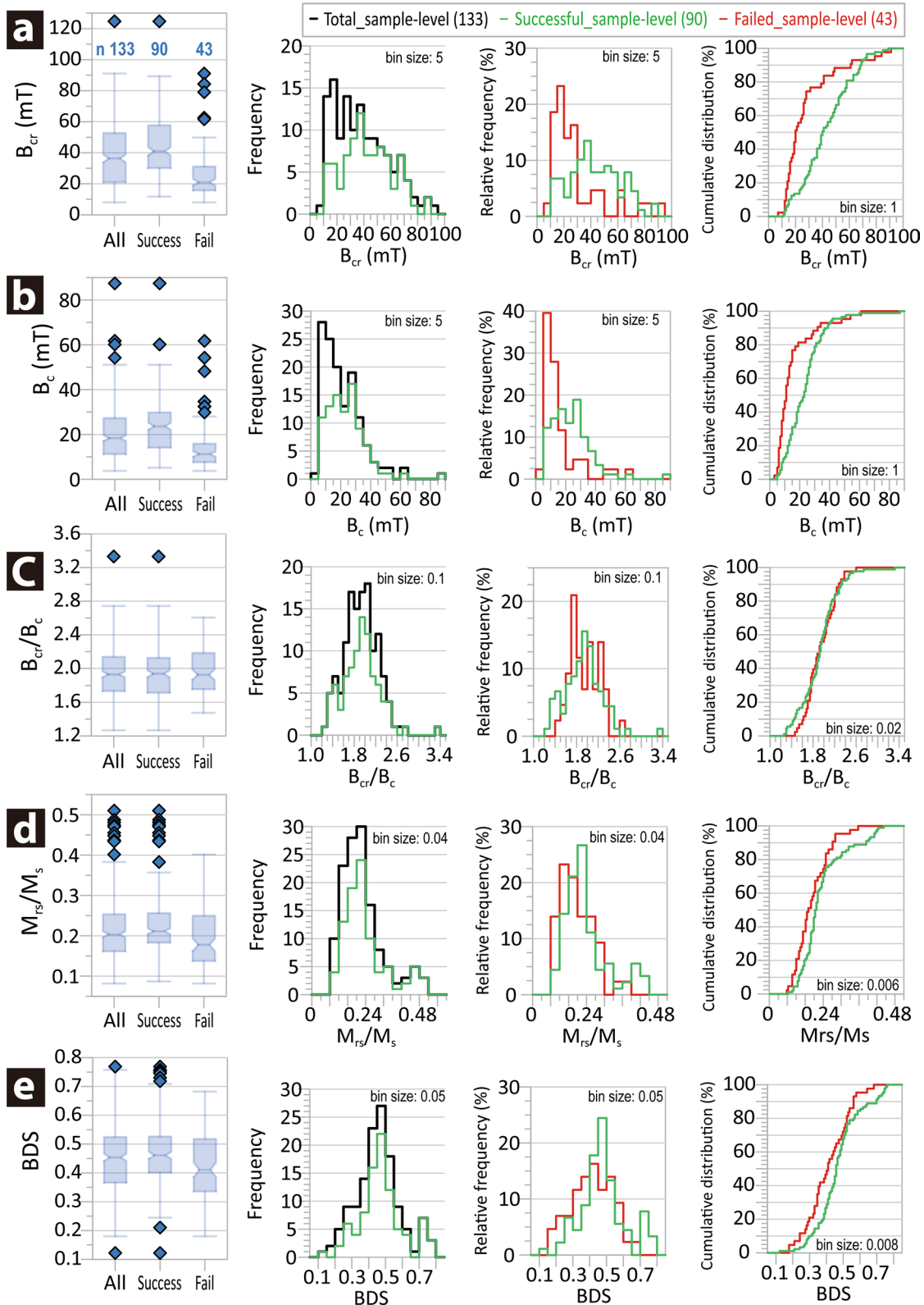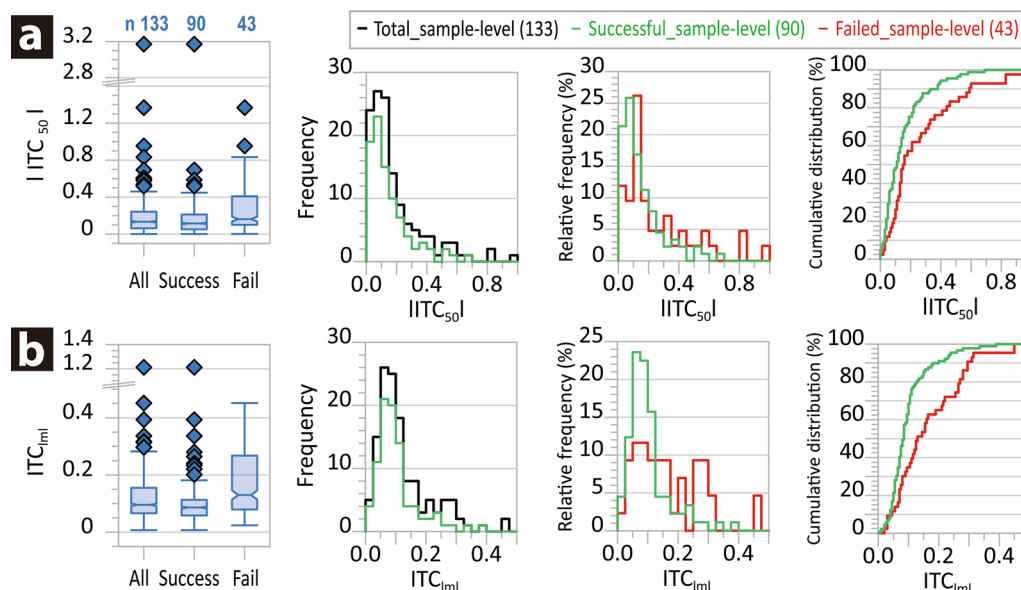
Fig. 7 (See legend on previous page.)

Ahn *et al. Earth, Planets and Space* (2024) 76:9

Page 21 of 29

Fig. 8 Comparisons of distributions in the respective M_s-T parameters, ITC_{50} (**a**) and $ITC_{|m|}$ (**b**), between the TS API "success" and "failure" data subsets. See Fig. 7 for detailed descriptions of these diagrams

Table 5 Summary of the Welch's t-test results of the TS API 'success' and 'failure' data subsets for the respective rock-magnetic parameters

	B_{cr}	B_c	B_{cr}/B_c	M_{rs}/M_s	BDS	$|ITC_{50}|$	$ITC_{|m|}$
t-statistic	4.1058	3.3377	−0.4374	2.9685	2.5690	−1.7983	−2.4247
p value (two-tailed)	0.0001	0.0013	*0.6627*	0.0037	0.0119	*0.0752*	0.0171

P < 0.05 indicates that the two datasets do not share the same mean, whereas *p ≥ 0.05* (in italic) indicates that it cannot discard sharing the same mean between the two datasets

consider them as another discrimination (i.e., preselection) tool in addition to the hysteresis parameters.

Previous studies have acknowledged several informative documentation using thermal changes in various rock-magnetic properties in a qualitative or quasi-quantitative manner to detect and filter out potentially erroneous (particularly low values) Thellier-type API determinations (to ensure or enhance the fidelity of API data). Nonetheless, using quantified parameters based on M_s-T curves to discuss relations to API results is rare, even in previous literature with Thellier-type API determinations; therefore, there is little parameter with a threshold available for reference. Several studies that used quantified parameters are briefly reviewed. Tanaka et al. (2007) used a measure of the difference between the starting and final M_s or k values in % of the starting value in either M_s-T or k-T curves with the criterion of < 15% for sample preselection for Thellier-type experiments. Qin et al. (2011) proposed a ratio using M_{rs}, the M_{rs} after a high temperature (480 °C) normalized by the initial M_{rs} at room temperature of

the pristine sample ($M_{rs480°C}/M_{rs25°C}$), with the criterion of $0.9 \leq M_{rs480°C}/M_{rs25°C} \leq 1.1$ to improve the reliability of Thellier-type API determinations. Tanaka and Kono (2002) and Kim et al. (2018) suggested a measure of the k difference (% of the pristine value) between the final values after each heating step during a Thellier-type experiment and the pristine value before the experiment, with the criterion that k differences throughout the experiment should be < 20%. These measures shared a common feature: only the initial and final values during the heating process were used in the calculation.

$ITC_{|m|}$ is a potential preselection criterion because it shows the tendency of more successful API results with decreasing $ITC_{|m|}$ values and a positive Welch's t-test ("Comparisons of distributions in rock-magnetic parameter between 'successful' and 'failed' TS API data" section). When considering a threshold value of 0.15 in $ITC_{|m|}$ slightly lower than 20% in the "success" samples loss, it permits ~76% in the success rate on our data compilation (Fig. 11d). Notably, the $ITC_{|m|}$ threshold value of 0.15 is similar to those of the other previously
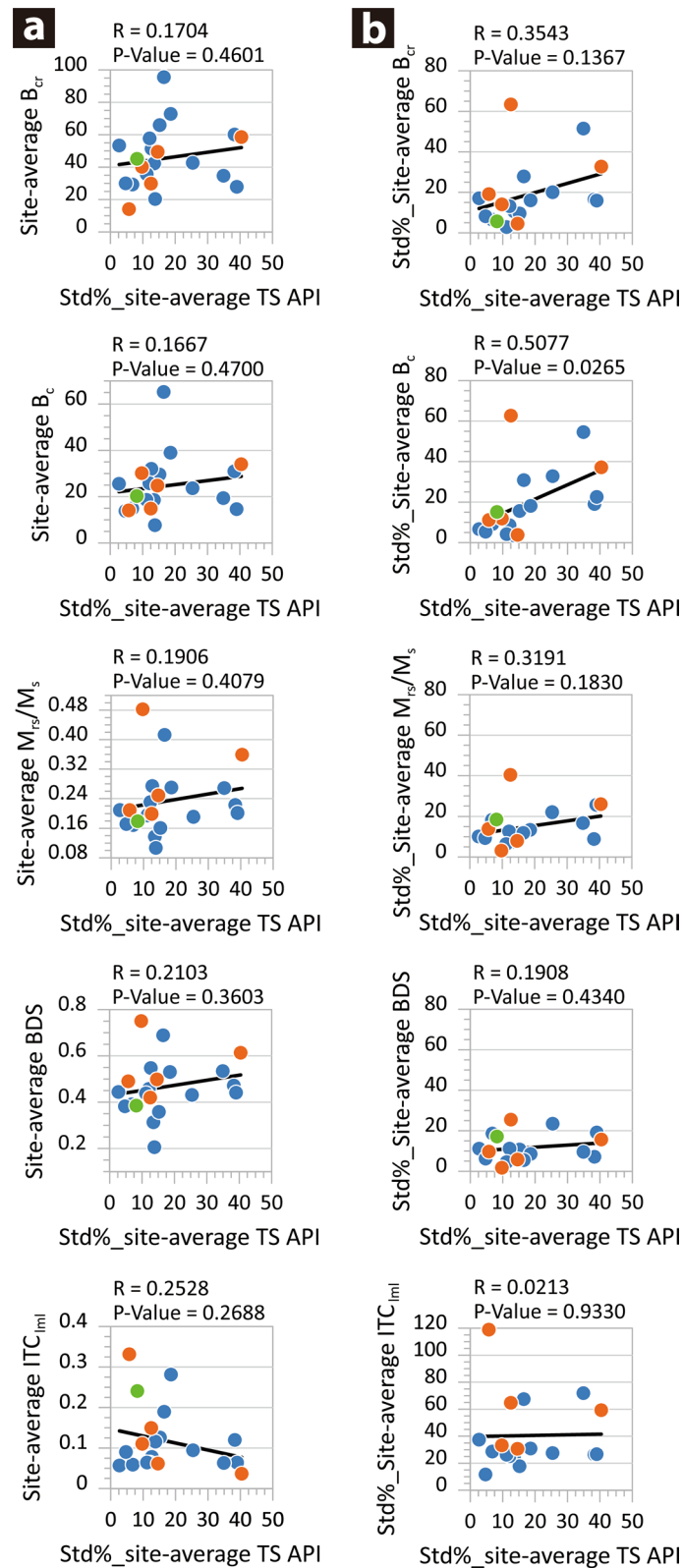
Fig. 9 Comparisons between TS API within-site standard deviation (%) and site-average (**a**) and within-site standard deviation (%) (**b**) of respective rock-magnetic parameters (B_{cr}, B_c, M_{rs}/M_s, BDS, and $ITC_{|m|}$). For each biplot of comparison, the correlation coefficient R and p value with a fit linear regression line (black line) are given. Light-blue, green, and orange circles indicate data points from Ethiopian Afar basalts (Ahn et al. 2016), Baengnyeong Island basalts (Ahn and Yamamoto 2019), and NE China volcanic field basalts (this study), respectively

Ahn *et al. Earth, Planets and Space*   (2024) 76:9

Page 23 of 29
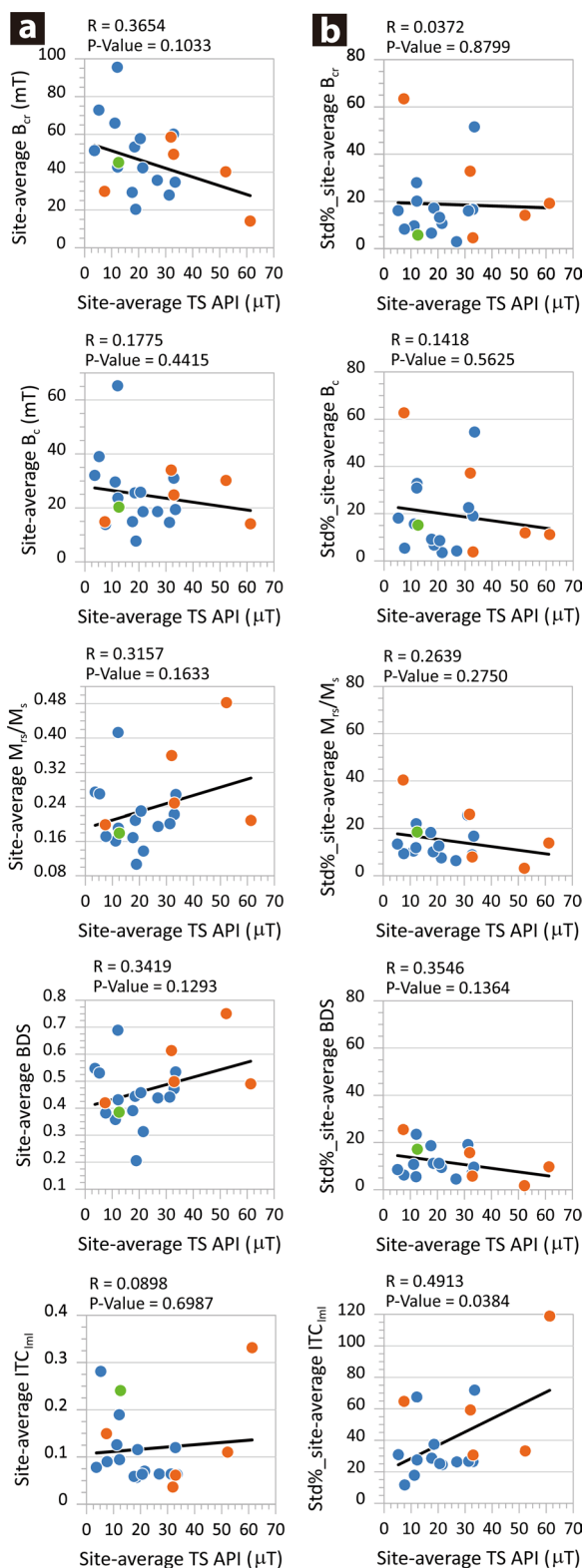
◀ **Fig. 10** Comparisons between site-average TS API and site-average (**a**) and within-site standard deviation (%) (**b**) of respective rock-magnetic parameters (B_{cr}, B_c, M_{rs}/M_s, BDS, and $ITC_{|m|}$). For each biplot of comparison, the correlation coefficient R and p value with a fit linear regression line (black line) are given. Representation of the data point colors is the same as that in Fig. 9

documented parameters for thermal changes in Thellier-type experiments (Tanaka and Kono 2002; Tanaka et al. 2007; Qin et al. 2011; Kim et al. 2018). $ITC_{|m|}$ offers better performance in preselection efficiency than M_{rs}/M_s or BDS but appears to be less sensitive than B_{cr} or B_c efficiency (Fig. 11).

Suggestion of the preselection criteria

Each hysteresis parameter B_c or B_{cr} and the M_s-T parameter $ITC_{|m|}$ can be used as a single efficient preselection criterion, revealing better efficiencies in B_c and B_{cr} than $ITC_{|m|}$. Furthermore, a combination of one hysteresis (B_c or B_{cr}) parameter and the other M_s-T curve ($ITC_{|m|}$) parameters can be used as a more efficient tool for preselection, given that there is no correlation between the hysteresis and M_s-T parameters. We consider two parameter combinations with the above-discussed threshold values as the preselection criteria, that is, $B_{cr} \geq 26$ mT and $ITC_{|m|} \leq 0.15$, and $B_c \geq 13$ mT and $ITC_{|m|} \leq 0.15$ (Fig. 12). One combined set of criteria, $B_{cr} \geq 26$ mT and $ITC_{|m|} \leq 0.15$, allows ~86% (65 of 76) in success rate in % of the screened "success" total, with ~28% (25 of 90) in the "success" samples loss rate (Fig. 12a). The other combined set, $B_c \geq 13$ mT and $ITC_{|m|} \leq 0.15$, allows ~85% (63 of 74) in the success rate and ~30% (27 of 90) in the "success" samples loss rate (Fig. 12b). We recommend a minimal set of $B_c \geq 13$ mT and $ITC_{|m|} \leq 0.15$, or of $B_{cr} \geq 26$ mT and $ITC_{|m|} \leq 0.15$ as preselection criteria.

Within-site dispersion of TS API estimates considering rock-magnetic parameters

Generally, the API determination for a site with high fidelity is achieved by averaging the API results from multiple samples/specimens. As stated in "Comparison between inter-sample dispersion of API determinations and rock-magnetic parameters for sites" section, the successful specimen-level TS API estimates in our data compilation allowed reasonably good within-site consistency in API averaging for most of the analyzed sites. We confirmed that unwanted, considerable API biases in site-averaged determination and within-site dispersion relying on inherent sample magnetic properties are less possible (Figs. 9 and 10).
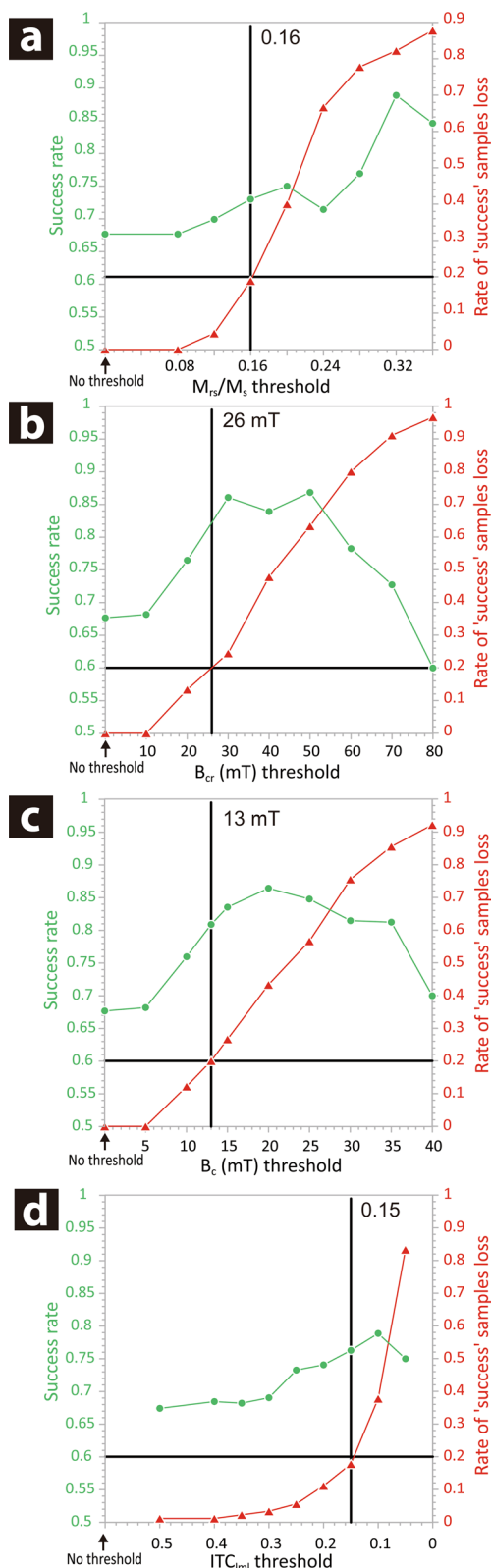
Fig. 11 Variations in ratio of the number of "success" TS API results of the samples preselected by the respective criterion to the total preselected ("success rate") and in the number of "success" results abandoned by the criterion to the total of "success" results/samples ("rate of the success samples loss") with different threshold values in the criterion for M_{rs}/M_s (**a**), B_{cr} (**b**), B_c (**c**), and $ITC_{|m|}$ (**d**). In each diagram, the horizontal line of 0.2 in rate of the success samples loss and vertical line of the respective rock-magnetic parameter value at 0.2 in rate of the success samples loss are given

However, for the sites 14181, DB15, DB12, DB(-1)B, and DB(-6), the individual TS API standard deviations were larger than 20% of the respective site averages, which is problematic in providing high-fidelity API site averages. At these sites, only the average of the whole API estimates is not believed to be an adequate API determination for a site. Specifically, we considered whether potentially biased TS API estimates within a site can be determined using rock-magnetic parameters. From the possible positive relationship between B_c and API within-site standard deviations (in %, Fig. 9), we suspect a possible B_c relevance to individual TS API estimates in the specimens of these sites. When considering this and our preselection criteria, the API estimates with $B_c < 13$ mT might be biased by potential rock-magnetic artefacts. Therefore, the high API estimate (16.6 µT) of sample DB15-2 (12.8 mT in B_c), the high API estimate (45.1 µT) of sample DB(-1)-3 (12.1 mT in B_c), and the low API estimate (25.9 µT) of sample DB(-6)-3 (12.1 mT in B_c) might be biased (Additional file 4: Table S2). Then, exclusion of these APIs in the site average determinations allows that DB15, DB(-1)B, and DB(-6) would yield API averages (~ 11 µT, ~ 24 µT, and ~ 37 µT, respectively) with better within-site consistency (cf. those listed in Additional file 7: Table S4). Extending another consideration relating to our preselection criteria, the low API estimate (21.0 µT) of sample DB12-2 with $ITC_{|m|} > 0.15$ (Additional file 4: Table S2) might be less faithful. Nonetheless, even these extended consideration does not allow the selection of the most likely estimates among the highly dispersed TS APIs for site 14181. Currently, the determined site-averaged API of site 14181 must be discarded due to being considered less faithful.

Conclusions

The TS experiment, which is becoming the most advanced and promising API determination technique, requires a systematic effort to link rock-magnetic parameters to TS API results to improve the quantitative
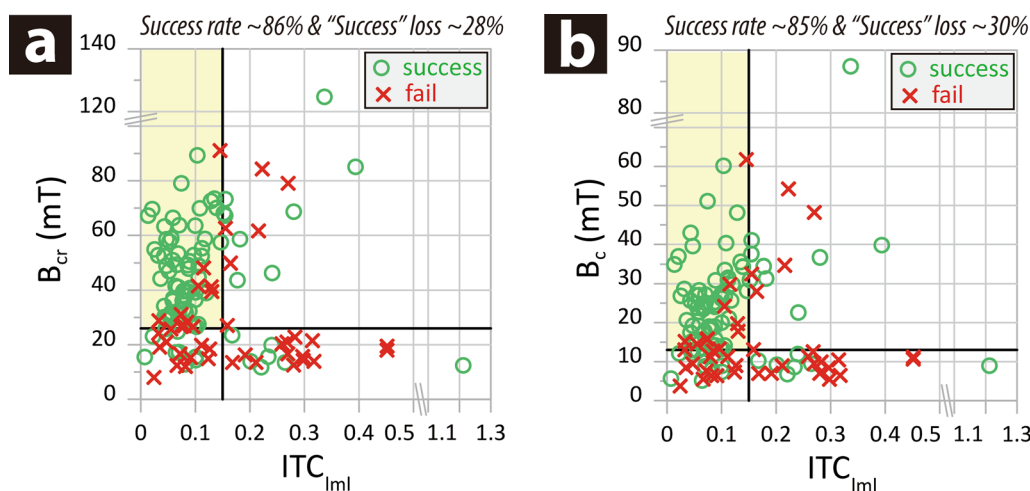
Fig. 12 Comparisons of combinations of one hysteresis (B_c or B_{cr}) and the other M_s-T curve ($ITC_{|m|}$) parameters between the TS API "success" and "failure" data subsets. (**a** and **b**) Biplots of B_{cr} vs. $ITC_{|m|}$ and B_c vs. $ITC_{|m|}$, respectively, with the consideration of when a minimal set comprising two different rock-magnetic parameters is adopted as the "sample priority selection criteria;" the proposed threshold values ($B_{cr} \geq 26$ mT and $ITC_{|m|} \leq 0.15$, and $B_c \geq 13$ mT, and $ITC_{|m|} \leq 0.15$, respectively; "Exploring 'ease-of-use' rock-magnetic parameters for the sample preselection criteria" section) of the two variables in each biplot are indicated by black solid lines; the pale yellow shaded zone of each biplot represents the zone distributed by data meeting the respective minimal set of criteria

success of API determination and API fidelity, as Thellier-type experiments have been most widely applied to date. Here, we explored the relationships between rock-magnetic parameters and TS API results (success or failure in determination and within-site consistency) using voluminous pairs (133 sample-level pairs from 38 different sites/cooling units) of sample-level rock-magnetic parameters and TS API data from late Cenozoic basaltic rocks. We addressed B_c, B_{cr}, B_{cr}/B_c, M_{rs}/M_s, and BDS values, and $|ITC_{50}|$ and $ITC_{|m|}$ values quantified from hysteresis measurements and thermomagnetic analysis with measurement rapidity and ubiquitous use.

Comparison of the hysteresis parameters to the API determination success or failure revealed that BDS and M_{rs}/M_s values more frequently addressed in previous literature were slightly higher for samples with "success" TS API results. Compared with BDS and M_{rs}/M_s, B_c and B_{cr} allowed more effective discrimination in distribution between "success" and "failure" samples; samples with lower B_c or B_{cr} displayed a higher failure rate of TS API determination. Comparison of the ITC parameters to the API determination success or failure revealed a visible relationship between $ITC_{|m|}$ and TS API success or failure. The success/failure discrimination by $ITC_{|m|}$ was more efficient than that by BDS or M_{rs}/M_s but less efficient than that by B_c or B_{cr}. We interpret that B_{cr}, B_c, and $ITC_{|m|}$ were individually available as parameters for the sample preselection criterion, with thresholds of $B_{cr} \geq 26$ mT, $B_c \geq 13$ mT, and $ITC_{|m|} \leq 0.15$, respectively. Moreover, the hysteresis (B_c or B_{cr}) and thermal change

($ITC_{|m|}$) parameters could be complementarily utilized, given the negligible relationship between them. This may be because $ITC_{|m|}$ is likely more sensitive to thermally induced magnetic changes. Hence, we suggest a minimal set of $B_c \geq 13$ mT (or $B_{cr} \geq 26$ mT) and $ITC_{|m|} \leq 0.15$ as the sample preselection criteria for quantitative success.

We also confirmed that the sample/specimen-level TS API estimates adopted through the TS experiment acceptance criteria and their derived site-average API values were generally unbiased or less biased by potential rock-magnetic artefacts. However, samples from sites with large within-site API dispersions might be associated with unwanted biases in individual TS API determination. Extended consideration based on our proposed preselection criteria might allow for the selection of more accurate API estimates from highly dispersed estimates within such a problematic site. However, if more faithful, unbiased API individuals cannot be salvaged, it should remain inconclusive in determining the site-averaged TS API.

In conclusion, the rapid-check rock-magnetic parameters implemented in this study can guarantee efficient acquisition and high fidelity of TS API data. Furthermore, we expect that the B_c (or B_{cr}) and $ITC_{|m|}$ parameters will also apply to Thellier-type experiments as efficient preselection criteria.

Abbreviations

AF(D)	Alternating field (demagnetization)
API	Absolute paleomagnetic field intensity

Ahn *et al. Earth, Planets and Space*   (2024) 76:9

Page 26 of 29

ARM	Anhysteretic remanent magnetization
B_c	Magnetic coercivity
B_{cr}	Remanence coercivity
BDS	Bulk domain stability
MaCRI	Marine Core Research Institute (Kochi University, Japan)
CRM	Chemical remanent magnetization
CT API experiment/method/protocol	Coe–Thellier API experiment/method/protocol
CVF	Changbaishan volcanic field
DC	Direct current
FORC	First-order reversal curve
ITC	Index of thermal change
JVF	Jingpohu volcanic field
k	Magnetic susceptibility
KIGAM	Korea Institute of Geoscience and Mineral Resources (South Korea)
LVF	Longgang volcanic field
MD	Multi-domain
M_{rs}	Saturation remanent magnetization
M_s	Saturation magnetization
M_s-T curve	Strong-field high-temperature thermomagnetic (induced saturation magnetization vs. temperature) curve
NE	Northeast
NRM	Natural remanent magnetization
PSD	Pseudo-single-domain
pTRM	Partial thermo-remanent magnetization
SD	Single-domain
T_c	Curie temperature
TCRM	Thermo-chemical remanent magnetization
TRM	Thermo-remanent magnetization
TS method/experiment/protocol	Tsunakawa–Shaw method/experiment/protocol

Supplementary Information

The online version contains supplementary material available at https://doi.org/10.1186/s40623-023-01953-x.

Additional file 1: Table S1. Summary of sample-level rock-magnetic parameters from hysteresis and M_s-T measurements of basalt samples from Northeast China (NE).

Additional file 2: Figure S1. First-order reversal curve (FORC) diagrams for the selected samples: 14,175-F, 14,181-G, 14,182-B, 14,183-C, and 14,222-F. Measurements parameters were set to B_{sat} = 100 mT, B_{c-max} = 110 mT, B_{u-max} = 50 mT, B_{u-min} = -50mT, averaging time = 200 ms, and 219 FORCs. To generate the diagram, the smoothing factor (SF) was set to 6 or 10 (output grid = 1). The associated plots of the B_{cr}/B_c and M_{rs}/M_s values in the Day plot are shown in Fig. 2b.

Additional file 3: Additional information note. Absolute paleomagnetic field intensity (API) determination using Coe's version of the Thellier-type (Coe–Thellier) method in a vacuum. See Additional files 8–12 for context.

Additional file 4: Table S2. Sample-level rock-magnetic parameters and additional information for Data Compilation were prepared in this study. n_hys, number of specimens used in magnetic hysteresis-related measurements; n_M_s-T, number of specimens used in M_s-T curve; Env_M_s-T, environment during M_s-T experiment (vac: vacuum); T_{max}_M_s-T, peak temperature during Ms-T experiment; Magnetic Mineral Category, classification based on the major magnetic mineral phase with T_c (Category I with no ≥ 400°C in T_c of the major phase, and Category II of the others); n_TS API, number of specimens applied to the Tsunakawa–Shaw (TS) API experiments; Success or Fail, "success" or "fail" in sample-level TS API result (if at least one successful result exists in a single sample, "success" is given). "*" denotes an average of the values from multiple results. "-" denotes "no data."

Additional file 5: Figure S2. Zijderveld orthogonal plot and associated intensity decay curve results obtained from the natural remanent magnetization (NRM) altering field (AF) demagnetization step during the TS experiment for representative specimens from eight sites of NE China volcanic field basalts. For each Zijderveld plot, filled and open circles indicate projections of data at temperature steps on the horizontal and vertical planes, respectively, and a characteristic remanence component (regarded as the primary remanence) determined in a high-AF level interval by principal component analysis is presented. Two "0" steps for a single demagnetization result indicate 'before the pre-treatment of low-temperature demagnetization (LTD)' and 'just after the LTD and before the AF demagnetization start'.

Additional file 6: Table S3. API site averages and associated standard deviations from the TS API results for NE China basalts. The site averages and standard deviations of the sample-level APIs are given only for each site where the number of sample-level API individuals is three or more. "-" denotes "not available". "n/N" denotes the numbers of specimen-level and sample-level TS API estimates determined successfully within a site, respectively.

Additional file 7: Table S4. Site averages and standard deviations (% of the site average) of the respective rock-magnetic parameters (with the magnetic mineral category) and TS API for sites with sample-level TS API estimates. Calculations of the presented values were performed using sample-level data from the Data Compilation. The data with "#" for site B1 were calculated exceptionally using, even together, sample-level data that are incompletely paired due to the loss of M_s-T data. "-" denotes "not applicable". The data are presented in Figs. 9 and 10.

Additional file 8: Figure S3. Representative specimen-level Coe–Thellier experiment (in a vacuum) For each specimen-level result, the Arai diagram (left) and Zijderveld orthogonal projection of the zero-field steps (NRMs) (right) in the specimen-coordinate systems are shown. In each Arai diagram, circles represent the pair of NRM and thermo-remanent magnetization (TRM) steps and triangles represent the partial TRM checks. Interpretations of the API determinations are provided in Supplementary Tables S3–S5 (see Sect. 4.1). For each orthogonal projection, the filled circles (open squares) show projections of the data at the temperature steps on the y–x (z–x) plane.

Additional file 9: Table S5. Summary of interpretations of the Coe–Thellier API results with the CCRIT criteria (Tauxe et al. 2016) using the "Paleointensity.org" online application (Béguin et al. 2020). Additional file 3: Supplementary information note provides more details.

Additional file 10: Table S6. Summary of interpretations of the Coe–Thellier API results with the RCRIT criteria (Sánchez-Moreno et al. 2020) using the "Paleointensity.org" online application (Béguin et al. 2020). Additional file 3: Supplementary information note provides more details.

Additional file 11: Table S7. Summary of interpretations of the Coe–Thellier API results with the modified PICRIT criteria (Paterson et al. 2014) using the "Paleointensity.org" online application (Béguin et al. 2020). Additional file 3: Supplementary information note provides more details.

Additional file 12: Table S8. Comparison of API determinations between the TS and Coe–Thellier (vacuum) methods with variable acceptance criteria. The TS API value for each sample was obtained from the result of a single specimen belonging to the sample, except for sample 14,181-E, which yielded a sample-level API value by calculating the mean value from the two specimen-level results. Each sample-level Coe–Thellier API value with certain criteria was obtained by averaging all API values that were calculated to meet certain criteria for a single specimen-level result.

Ahn *et al. Earth, Planets and Space*   (2024) 76:9

Page 27 of 29

Author contributions

Funding

Availability of data and materials
Data are available from the corresponding author on reasonable request.

Declarations

Competing interests
The authors declare that they have no competing interests.

Author details
[1]Quaternary Environment Research Center, Climate Change Response Division, Korea Institute of Geoscience and Mineral Resources (KIGAM), Daejeon 34132, Republic of Korea. [2]Division of Environmental Science and Engineering, Pohang University of Science and Technology (POSTECH), Pohang 37673, Republic of Korea. [3]Marine Core Research Institute (MaCRI), Kochi University, Kochi 783-8502, Japan.

References

Ahn H-S, Yamamoto Y (2019) Paleomagnetic study of basaltic rocks from Baengnyeong Island, Korea: efficiency of the Tsunakawa‒Shaw pale-ointensity determination on non-SD-bearing materials and implication for the early Pliocene geomagnetic field intensity. Earth Planets Space 71(1):126. https://doi.org/10.1186/s40623-019-1107-6

Ahn H-S, Kidane T, Yamamoto Y, Otofuji Y-i (2016) Low geomagnetic field intensity in the Matuyama Chron: palaeomagnetic study of a lava sequence from Afar depression. East Afr Geophys J Int 204(1):127–146. https://doi.org/10.1093/gji/ggv303

Aitken MJ, Allsop AL, Bussell GD, Winter MB (1988) Determination of the inten-sity of the Earth's magnetic field during archaeological times: reliability of the thellier technique. Rev Geophys 26(1):3–12. https://doi.org/10.1029/RG026i001p00003

Béguin A, Paterson GA, Biggin AJ, de Groot LV (2020) Paleointensity.org: an online, open source, application for the interpretation of paleointensity data. Geochem Geophys Geosyst 21(5):e2019GC008791. https://doi.org/10.1029/2019GC008791

Bono RK, Tarduno JA, Nimmo F, Cottrell RD (2019) Young inner core inferred from Ediacaran ultra-low geomagnetic field intensity. Nat Geosci 12(2):143–147. https://doi.org/10.1038/s41561-018-0288-0

Calvo M, Prévot M, Perrin M, Riisager J (2002) Investigating the reasons for the failure of palaeointensity experiments: a study on historical lava flows

from Mt. Etna (Italy). Geophys J Int 149:44–63. https://doi.org/10.1046/j.1365-246X.2002.01619.x

Carvallo C, Roberts AP, Leonhardt R, Laj C, Kissel C, Perrin M, Camps P (2006) Increasing the efficiency of paleointensity analyses by selection of samples using first-order reversal curve diagrams. J Geophys Res Solid Earth. https://doi.org/10.1029/2005JB004126

Choi SH, Mukasa SB, Kwon S-T, Andronikov AV (2006) Sr, Nd, Pb and Hf isotopic compositions of late Cenozoic alkali basalts in South Korea: evidence for mixing between the two dominant asthenospheric mantle domains beneath East Asia. Chem Geol 232(3):134–151. https://doi.org/10.1016/j.chemgeo.2006.02.014

Chun J-H, Cheong D (2020) Origin of compositional diversity of marine tephra during the late Middle Pleistocene B-KY1 Baekdusan volcanic eruption. Appl Sci 10(13):4469. https://doi.org/10.3390/app10134469

Coe RS (1967) Paleo-intensities of the Earth's magnetic field determined from Tertiary and Quaternary rocks. J Geophys Res (1896–1977) 72(12):3247–3262. https://doi.org/10.1029/JZ072i012p03247

Coe RS, Grommé S, Mankinen EA (1978) Geomagnetic paleointensities from radiocarbon-dated lava flows on Hawaii and the question of the Pacific nondipole low. J Geophys Res Solid Earth 83(B4):1740–1756. https://doi.org/10.1029/JB083iB04p01740

Cooper A, Turney CSM, Palmer J, Hogg A, McGlone M, Wilmshurst J, Lorrey AM, Heaton TJ, Russell JM, McCracken K, Anet JG, Rozanov E, Friedel M, Suter I, Peter T, Muscheler R, Adolphi F, Dosseto A, Faith JT, Fenwick P, Fogwill CJ, Hughen K, Lipson M, Liu J, Nowaczyk N, Rainsley E, Bronk Ramsey C, Sebastianelli P, Souilmi Y, Stevenson J, Thomas Z, Tobler R, Zech R (2021) A global environmental crisis 42,000 years ago. Science 371(6531):811–818. https://doi.org/10.1126/science.abb8677

Courtillot V, Gallet Y, Le Mouël J-L, Fluteau F, Genevey A (2007) Are there con-nections between the Earth's magnetic field and climate? Earth Planet Sci Lett 253(3):328–339. https://doi.org/10.1016/j.epsl.2006.10.032

Cromwell G, Tauxe L, Halldórsson SA (2015) New paleointensity results from rapidly cooled Icelandic lavas: implications for Arctic geomagnetic field strength. J Geophys Res Solid Earth 120(5):2913–2934. https://doi.org/10.1002/2014JB011828

Day R, Fuller M, Schmidt VA (1977) Hysteresis properties of titanomagnetites: grain-size and compositional dependence. Phys Earth Planet Inter 13:260–267. https://doi.org/10.1016/0031-9201(77)90108-X

Dekkers MJ, Böhnel HN (2006) Reliable absolute palaeointensities independ-ent of magnetic domain state. Earth Planet Sci Lett 248(1):508–517. https://doi.org/10.1016/j.epsl.2006.05.040

Di Chiara A, Muxworthy AR, Trindade RIF, Bispo-Santos F (2017) Paleopro-terozoic geomagnetic field strength from the Avanavero mafic sills, Amazonian Craton, Brazil. Geochem Geophys Geosyst 18:3891–3903. https://doi.org/10.1002/2017GC007175

Dunlop DJ (2002a) Theory and application of the Day plot (Mrs/Ms versus Hcr/Hc) 1. Theoretical curves and tests using titanomagnetite data. J Geophys Res. https://doi.org/10.1029/2001JB000486

Dunlop DJ (2002b) Theory and application of the day plot (Mrs/Ms versus Hcr/Hc) 2. Application to data for rocks, sediments, and soils. J Geophys Res Solid Earth. https://doi.org/10.1029/2001JB000487

Fukuma K (2023) Testing determinations of Thellier paleointensities on 1962 and 1983 lava flows and scoriae in Miyakejima, Japan. Earth Planets Space 75(1):27. https://doi.org/10.1186/s40623-023-01781-z

Gee JS, Yu Y, Bowles J (2010) Paleointensity estimates from ignimbrites: an evaluation of the Bishop Tuff. Geochem Geophys Geosyst. https://doi.org/10.1029/2009GC002834

Genevey A, Gallet Y, Thébault E, Livermore PW, Fournier A, Jesset S, Lefèvre A, Mahé-Hourlier N, Marot E, Regnard S (2021) Archeomagnetic intensity investigations of French medieval ceramic workshops: contribution to regional field modeling and archeointensity-based dating. Phys Earth Planet Inter 318:106750. https://doi.org/10.1016/j.pepi.2021.106750

Grommé CS, Wright TL, Peck DL (1969) Magnetic properties and oxidation of iron-titanium oxide minerals in Alae and Makaopuhi Lava Lakes, Hawaii. J Geophys Res 74(22):5277–5293. https://doi.org/10.1029/JB074i022p05277

Haag M, Dunn JR, Fuller M (1995) A new quality check for absolute palaeoin-tensities of the Earth magnetic field. Geophys Res Lett 22(24):3549–3552. https://doi.org/10.1029/95GL03333

Harrison RJ, Feinberg JM (2008) FORCinel: an improved algorithm for calculat-ing first-order reversal curve distributions using locally weighted

Ahn *et al. Earth, Planets and Space*   (2024) 76:9

Page 28 of 29

regression smoothing. Geochem Geophys Geosyst 9(5):Q05016. https://doi.org/10.1029/2008GC001987

Hill MJ, Shaw J (2000) Magnetic field intensity study of the 1960 Kilauea lava flow, Hawaii, using the microwave palaeointensity technique. Geophys J Int 142(2):487–504. https://doi.org/10.1046/j.1365-246x.2000.00164.x

Hrouda F (2003) Indices for numerical characterization of the alteration processes of magnetic minerals taking place during investigation of temperature variation of magnetic susceptibility. Stud Geophys Geod 47(4):847–861. https://doi.org/10.1023/A:1026398920172

Hrouda F, Chlupáčová M, Novák JK (2002) Variations in magnetic anisotropy and opaque mineralogy along a kilometer deep profile within a vertical dyke of the syenogranite porphyry at Ćínovec (Czech Republic). J Volcanol Geoth Res 113(1):37–47. https://doi.org/10.1016/S0377-0273(01)00249-9

Jeong D, Liu Q, Yamamoto Y, Yu Y, Zhao X, Qin H (2021) New criteria for selecting reliable Thellier-type paleointensity results from the 1960 Kilauea lava flows, Hawaii. Earth Planets Space 73(1):144. https://doi.org/10.1186/s40623-021-01473-6

Kato C, Sato M, Yamamoto Y, Tsunakawa H, Kirschvink JL (2018) Paleomagnetic studies on single crystals separated from the middle Cretaceous Iritono granite. Earth Planets Space 70(1):176. https://doi.org/10.1186/s40623-018-0945-y

Kim W, Doh S-J, Yu Y (2018) Reliable paleointensity determinations from Late Cretaceous volcanic rocks in Korea with constraint of thermochemical alteration. Phys Earth Planet Inter 279:47–56. https://doi.org/10.1016/j.pepi.2018.04.004

Kirschvink J (1980) The least-squares line and plane and the analysis of palaeomagnetic data. Geophys J Int 62(3):699–718. https://doi.org/10.1111/j.1365-246X.1980.tb02601.x

Kissel C, Laj C (2004) Improvements in procedure and paleointensity selection criteria (PICRIT-03) for Thellier and Thellier determinations: application to Hawaiian basaltic long cores. Phys Earth Planet Inter 147(2):155–169. https://doi.org/10.1016/j.pepi.2004.06.010

Kitaba I, Hyodo M, Katoh S, Matsushita M (2012) Phase-lagged warming and the disruption of climatic rhythms during the Matuyama-Brunhes magnetic polarity transition. Gondwana Res 21(2):595–600. https://doi.org/10.1016/j.gr.2011.07.005

Kitaba I, Hyodo M, Nakagawa T, Katoh S, Dettman DL, Sato H (2017) Geological support for the umbrella effect as a link between geomagnetic field and climate. Sci Rep 7(1):40682. https://doi.org/10.1038/srep40682

Kitahara Y, Yamamoto Y, Ohno M, Kuwahara Y, Kameda S, Hatakeyama T (2018) Archeointensity estimates of a tenth-century kiln: first application of the Tsunakawa-Shaw paleointensity method to archeological relics. Earth Planets Space 70(1):79. https://doi.org/10.1186/s40623-018-0841-5

Kitahara Y, Nishiyama D, Ohno M, Yamamoto Y, Kuwahara Y, Hatakeyama T (2021) Construction of new archaeointensity reference curve for East Asia from 200 CE to 1100 CE. Phys Earth Planet Inter 310:106596. https://doi.org/10.1016/j.pepi.2020.106596

Knudsen MF, Riisager P (2009) Is there a link between Earth's magnetic field and low-latitude precipitation? Geology 37(1):71–74. https://doi.org/10.1130/g25238a.1

Le Goff M, Gallet Y (2004) A new three-axis vibrating sample magnetometer for continuous high-temperature magnetization measurements: applications to paleo- and archeo-intensity determinations. Earth Planet Sci Lett 229(1):31–43. https://doi.org/10.1016/j.epsl.2004.10.025

Lee YS, Kodama K (2009) A possible link between the geomagnetic field and catastrophic climate at the Paleocene-Eocene thermal maximum. Geology 37(11):1047–1050. https://doi.org/10.1130/g30190a.1

Lee SH, Oh CW, Lee YS, Lee S-G, Liu J-q (2021) Petrogenesis of the Cenozoic volcanic rocks in Baekdu volcano in northeastern Asia and the expected depth of the magma chamber based on geochemistry, mineral chemistry, and Sr-Nd-Pb isotope chemistry. Lithos 388–389:106080. https://doi.org/10.1016/j.lithos.2021.106080

Leonhardt R, Heunemann C, Krása D (2004) Analyzing absolute paleointensity determinations: acceptance criteria and the software ThellierTool4.0. Geochem Geophys Geosyst. https://doi.org/10.1029/2004GC000807

Liu JQ (1983) Changbai Mountains Cenozoic volcanic activity. Master's Proceedings of Geology Institute. Science and Technology Press, Beijing, pp. 343–355. (in Chinese with English abstract)

Liu JQ (1987) Study on geochronology of the Cenozoic volcanic rocks in northeast China. Acta Petrologica Sinica 4:22–31

Liu JQ (1988) Volcanic episodes of the Cenozoic in northeast China regions. Acta Petrologica Sinica 2:1–9

Liu B, Chen Y, Zhu B (1989) Origin of Cenozoic basalts from Jingbohu, Northeast China and chemical characteristics of their mantle source—Sr–Pb isotope and trace element evidence. Acta Petrologica Sinica 1:9–19

Liu J, Han J, Fyfe WS (2001) Cenozoic episodic volcanism and continental rifting in northeast China and possible link to Japan Sea development as revealed from K-Ar geochronology. Tectonophysics 339(3):385–401. https://doi.org/10.1016/S0040-1951(01)00132-9

Lloyd SJ, Paterson GA, Thallner D, Biggin AJ (2021) Improvements to the Shaw-type absolute palaeointensity method. Front Earth Sci. https://doi.org/10.3389/feart.2021.701863

Marshall M, Cox A (1971) Effect of oxidation on the natural remanent magnetization of titanomagnetite in suboceanic basalt. Nature 230(5288):28–31. https://doi.org/10.1038/230028a0

Mochizuki N, Tsunakawa H, Oishi Y, Wakai S, Wakabayashi K-i, Yamamoto Y (2004) Palaeointensity study of the Oshima 1986 lava in Japan: implications for the reliability of the Thellier and LTD-DHT Shaw methods. Phys Earth Planet Inter 146(3):395–416. https://doi.org/10.1016/j.pepi.2004.02.007

Mochizuki N, Tsunakawa H, Shibuya H, Cassidy J, Smith IEM (2006) Palaeointensities of the Auckland geomagnetic excursions by the LTD-DHT Shaw method. Phys Earth Planet Inter 154(2):168–179. https://doi.org/10.1016/j.pepi.2005.09.005

Mochizuki N, Oda H, Ishizuka O, Yamazaki T, Tsunakawa H (2011) Paleointensity variation across the Matuyama-Brunhes polarity transition: observations from lavas at Punaruu Valley, Tahiti. J Geophys Res Solid Earth. https://doi.org/10.1029/2010JB008093

Mochizuki N, Maruuchi T, Yamamoto Y, Shibuya H (2013) Multi-level consistency tests in paleointensity determinations from the welded tuffs of the Aso pyroclastic-flow deposits. Phys Earth Planet Inter 223:40–54. https://doi.org/10.1016/j.pepi.2013.05.001

Mochizuki N, Fujii S, Hasegawa T, Yamamoto Y, Hatakeyama T, Yamashita D, Okada M, Shibuya H (2021) A tephra-based approach to calibrating relative geomagnetic paleointensity stacks to absolute values. Earth Planet Sci Lett 572:117119. https://doi.org/10.1016/j.epsl.2021.117119

Nagata T (1953) Rock magnetism, 1st edn. Maruzen Company, Tokyo, pp 123–192

Nagata T, Arai Y, Momose K (1963) Secular variation of the geomagnetic total force during the last 5000 years. J Geophys Res (1896–1977) 68(18):5277–5281. https://doi.org/10.1029/j.2156-2202.1963.tb00005.x

Nitta H, Saito T, Shitaoka Y (2020) Recent eruption history inferred from eruption ages of the two latest lava flows using multi-dating at Yokodake Volcano, Japan. Earth Planets Space 72(1):103. https://doi.org/10.1186/s40623-020-01220-3

Oishi Y, Tsunakawa H, Mochizuki N, Yamamoto Y, Wakabayashi K-I, Shibuya H (2005) Validity of the LTD-DHT Shaw and Thellier palaeointensity methods: a case study of the Kilauea 1970 lava. Phys Earth Planet Inter 149(3):243–257. https://doi.org/10.1016/j.pepi.2004.10.009

Okayama K, Mochizuki N, Wada Y, Otofuji Y-i (2019) Low absolute paleointensity during Late Miocene Noma excursion of the Earth's magnetic field. Phys Earth Planet Inter 287:10–20. https://doi.org/10.1016/j.pepi.2018.12.006

Özdemir Ö, Dunlop DJ (1985) An experimental study of chemical remanent magnetizations of synthetic monodomain titanomaghemites with initial thermoremanent magnetizations. J Geophys Res 90:11513–11523. https://doi.org/10.1029/JB090iB13p11513

Paterson GA, Muxworthy AR, Roberts AP, Mac Niocaill C (2010) Assessment of the usefulness of lithic clasts from pyroclastic deposits for paleointensity determination. J Geophys Res Solid Earth. https://doi.org/10.1029/2009JB006475

Paterson GA, Tauxe L, Biggin AJ, Shaar R, Jonestrask LC (2014) On improving the selection of Thellier-type paleointensity data. Geochem Geophys Geosyst 15(4):1180–1192. https://doi.org/10.1002/2013GC005135

Paterson GA, Muxworthy AR, Yamamoto Y, Pan Y (2017) Bulk magnetic domain stability controls paleointensity fidelity. Proc Natl Acad Sci 114(50):13120–13125. https://doi.org/10.1073/pnas.1714047114

Pérez-Rodríguez N, Morales J, Goguitchaichvili A, García-Tenorio F (2019) A comprehensive paleomagnetic study from the last Plinian eruptions of Popocatepetl volcano: absolute chronology of lavas and estimation

Ahn *et al. Earth, Planets and Space*   (2024) 76:9

Page 29 of 29

of emplacement temperatures of PDCs. Earth Planets Space 71(1):80. https://doi.org/10.1186/s40623-019-1059-x

Pérez-Rodríguez N, Morales J, Cejudo R, Guilbaud M-N, Goguitchaichvili A (2022) Reassessing the paleointensities of three Quaternary volcanic structures of the -Michoacán-Guanajuato Volcanic Field (Mexico) through a multimethodological analysis. Phys Earth Planet Inter 332:106927. https://doi.org/10.1016/j.pepi.2022.106927

Prévot M, Mankinen EA, Coe RS, Grommé CS (1985) The Steens Mountain (Oregon) geomagnetic polarity transition: 2. Field intensity variations and discussion of reversal models. J Geophys Res Solid Earth 90:10417–10448. https://doi.org/10.1029/JB090iB12p10417

Qin H, He H, Liu QS, Cai S (2011) Paleointensity just at the onset of the Cretaceous normal superchron. Phys Earth Planet Inter 187(3–4):199–211. https://doi.org/10.1016/jpepi.2011.05.009

Riisager P, Riisager J (2001) Detecting multidomain magnetic grains in Thellier palaeointensity experiments. Phys Earth Planet Inter 125(1):111–117. https://doi.org/10.1016/S0031-9201(01)00236-9

Roberts AP, Heslop D, Zhao X, Pike CR (2014) Understanding fine magnetic particle systems through use of first-order reversal curve diagrams. Rev Geophys 52(4):557–602. https://doi.org/10.1002/2014RG000462

Roberts AP, Tauxe L, Heslop D, Zhao X, Jiang Z (2018a) A critical appraisal of the "Day" diagram. J Geophys Res Solid Earth 123(4):2618–2644. https://doi.org/10.1002/2017JB015247

Roberts AP, Zhao X, Harrison RJ, Heslop D, Muxworthy AR, Rowan CJ, Larrasoaña J-C, Florindo F (2018b) Signatures of reductive magnetic mineral diagenesis from unmixing of first-order reversal curves. J Geophys Res Solid Earth 123(6):4500–4522. https://doi.org/10.1029/2018JB015706

Rolph TC, Shaw J (1985) A new method of paleofield magnitude correction for thermally altered samples and its application to lower carboniferous lavas. Geophys J R Astron Soc 80:773–781. https://doi.org/10.1111/j.1365-246X.1985.tb05124.x

Sánchez-Moreno EM, Calvo-Rathert M, Goguitchaichvili A, Tauxe L, Vashakidze GT, Lebedev VA (2020) Weak palaeointensity results over a Pliocene volcanic sequence from Lesser Caucasus (Georgia): transitional record or time averaged field? Geophys J Int 220(3):1604–1618. https://doi.org/10.1093/gji/ggz533

Santos CN, Tauxe L (2019) Investigating the accuracy, precision, and cooling rate dependence of laboratory-acquired thermal remanences during paleointensity experiments. Geochem Geophys Geosyst 20(1):383–397. https://doi.org/10.1029/2018GC007946

Shaar R, Tauxe L (2013) Thellier GUI: an integrated tool for analyzing paleointensity data from Thellier-type experiments. Geochem Geophys Geosyst 14(3):677–692. https://doi.org/10.1002/ggge.20062

Shaw J (1974) A new method of determining the magnitude of the palaeomagnetic field: application to five historic lavas and five archaeological samples. Geophys J Roy Astron Soc 76:637–651. https://doi.org/10.1111/j.1365-246X.1974.tb05443.x

Singer BS, Jicha BR, Mochizuki N, Coe RS (2019) Synchronizing volcanic, sedimentary, and ice core records of Earth's last magnetic polarity reversal. Sci Adv 5(8):eaaw4621. https://doi.org/10.1126/sciadv.aaw4621

Smirnov AV, Tarduno JA (2003) Magnetic hysteresis monitoring of Cretaceous submarine basaltic glass during Thellier paleointensity experiments: evidence for alteration and attendant low field bias. Earth Planet Sci Lett 206(3):571–585. https://doi.org/10.1016/S0012-821X(02)01123-8

Suter I, Zech R, Anet JG, Peter T (2014) Impact of geomagnetic excursions on atmospheric chemistry and dynamics. Clim past 10(3):1183–1194. https://doi.org/10.5194/cp-10-1183-2014

Tanaka H, Kono M (2002) Paleointensities from a Cretaceous basalt platform in Inner Mongolia, northeastern China. Phys Earth Planet Inter 133(1):147–157. https://doi.org/10.1016/S0031-9201(02)00091-2

Tanaka H, Takahashi N, Zheng Z (2007) Paleointensities from Tertiary basalts, Inner Mongolia and Hebei Province, northeastern China. Earth Planets Space 59(7):747–754. https://doi.org/10.1186/BF03352737

Tarduno JA, Cottrell RD, Davis WJ, Nimmo F, Bono RK (2015) A hadean to paleoarchean geodynamo recorded by single zircon crystals. Science 349(6247):521–524. https://doi.org/10.1126/science.aaa9114

Tauxe L, Shaar R, Jonestrask L, Swanson-Hysell NL, Minnett R, Koppers AAP, Constable CG, Jarboe N, Gaastra K, Fairchild L (2016) PmagPy: software package for paleomagnetic data analysis and a bridge to the Magnetics Information Consortium (MagIC) database. Geochem Geophys Geosyst 17(6):2450–2463. https://doi.org/10.1002/2016GC006307

Thellier É, Thellier O (1959) Sur l'intensité du champ magnétique terrestre dans le passé historique et géologique. Annales Géophysique 15:285–376

Tsunakawa H, Shaw J (1994) The Shaw method of palaeointensity determinations and its application to recent volcanic rocks. Geophys J Int 118(3):781–787. https://doi.org/10.1111/j.1365-246X.1994.tb03999.x

Tsunakawa H, Wakabayashi K-i, Mochizuki N, Yamamoto Y, Ishizaka K, Hirata T, Takahashi F, Seita K (2009) Paleointensity study of the middle Cretaceous Iritono granite in northeast Japan: implication for high field intensity of the Cretaceous normal superchron. Phys Earth Planet Inter 176(3):235–242. https://doi.org/10.1016/j.pepi.2009.07.001

Wang H, Kent DV (2013) A paleointensity technique for multidomain igneous rocks. Geochem Geophys Geosyst 14(10):4195–4213. https://doi.org/10.1002/ggge.20248

Wang HF, Yang XC, Zhu BQ, Fan SK, Dai TM (1988) K-Ar chronology and evolution of the Cenozoic volcanic rocks in the eastern China. Geochimica 3:1–11

Wei H, Wang Y, Jin J, Gao L, Yun S-H, Jin B (2007) Timescale and evolution of the intracontinental Tianchi volcanic shield and ignimbrite-forming eruption, Changbaishan, Northeast China. Lithos 96(1):315–324. https://doi.org/10.1016/j.lithos.2006.10.004

Wei H, Liu G, Gill J (2013) Review of eruptive activity at Tianchi volcano, Changbaishan, northeast China: implications for possible future eruptions. Bull Volcanol 75(4):706. https://doi.org/10.1007/s00445-013-0706-5

Yamamoto Y, Hoshi H (2008) Paleomagnetic and rock magnetic studies of the Sakurajima 1914 and 1946 andesitic lavas from Japan: a comparison of the LTD-DHT Shaw and Thellier paleointensity methods. Phys Earth Planet Inter 167(1):118–143. https://doi.org/10.1016/j.pepi.2008.03.006

Yamamoto Y, Tsunakawa H (2005) Geomagnetic field intensity during the last 5 Myr: LTD-DHT Shaw palaeointensities from volcanic rocks of the Society Islands, French Polynesia. Geophys J Int 162(1):79–114. https://doi.org/10.1111/j.1365-246X.2005.02651.x

Yamamoto Y, Yamaoka R (2018) Paleointensity study on the Holocene surface lavas on the island of Hawaii using the Tsunakawa-Shaw method. Front Earth Sci. https://doi.org/10.3389/feart.2018.00048

Yamamoto Y, Tsunakawa H, Shibuya H (2003) Palaeointensity study of the Hawaiian 1960 lava: implications for possible causes of erroneously high intensities. Geophys J Int 153(1):263–276. https://doi.org/10.1046/j.1365-246X.2003.01909.x

Yamamoto Y, Torii M, Natsuhara N (2015) Archeointensity study on baked clay samples taken from the reconstructed ancient kiln: implication for validity of the Tsunakawa-Shaw paleointensity method. Earth Planets Space 67(1):63. https://doi.org/10.1186/s40623-015-0229-8

Yamamoto Y, Tauxe L, Ahn H, Santos C (2022) Absolute paleointensity experiments on aged thermoremanent magnetization: assessment of reliability of the Tsunakawa-Shaw and other methods with implications for "fragile" curvature. Geochem Geophys Geosyst 23(4):e2022GC010391. https://doi.org/10.1029/2022GC010391

Yan J, Zhao J-X (2008) Cenozoic alkali basalts from Jingpohu, NE China: the role of lithosphere–asthenosphere interaction. J Asian Earth Sci 33(1):106–121. https://doi.org/10.1016/j.jseaes.2007.11.001

Yoshimura Y, Yamazaki T, Yamamoto Y, Ahn H-S, Kidane T, Otofuji Y-i (2020) Geomagnetic paleointensity around 30 Ma estimated from Afro-Arabian large igneous province. Geochem Geophys Geosyst 21(12):e2020GC009341. https://doi.org/10.1029/2020GC009341

Yu Y, Tauxe L, Genevey A (2004) Toward an optimal geomagnetic field intensity determination technique. Geochem Geophys Geosyst. https://doi.org/10.1029/2003GC000630

Zhang Y, Swanson-Hysell NL, Avery MS, Fu RR (2022) High geomagnetic field intensity recorded by anorthosite xenoliths requires a strongly powered late Mesoproterozoic geodynamo. Proc Natl Acad Sci 119(29):e2202875119. https://doi.org/10.1073/pnas.2202875119

Zhou T, Tarduno JA, Nimmo F, Cottrell RD, Bono RK, Ibanez-Mejia M, Huang W, Hamilton M, Kodama K, Smirnov AV, Crummins B, Padgett F (2022) Early Cambrian renewal of the geodynamo and the origin of inner core structure. Nat Commun 13(1):4161. https://doi.org/10.1038/s41467-022-31677-7

Publisher's Note